Technical Physics, 2022, Vol. 67, No. 10

15

Section methods of X-Ray diffraction topography

© I.L. Shul'pina,[1] E.V. Suvorov,[2] I.A. Smirnova,[2] T.S. Argunova[1]

[1] Ioffe Institute, St. Petersburg, Russia
[2] Osipyan Institute of Solid State Physics RAS Russian Academy of Sciences, Chernogolovka, Moscow District, Russia
e-mail: argunova@mail.ioffe.ru

Received March 18, 2022
Revised June 7, 2022
Accepted June 10, 2022

X-ray topography is a group of methods for obtaining diffraction images of structural defects in crystals. Among them, section topography techniques are distinguished by their abilities in acquiring quantitative information about defects based on the analysis of the images. For this purpose, special applications of the dynamic theory of X-ray diffraction are being developed. The interference of wave fields excited in a crystal by an X-ray beam is the basis of the section methods. Their sensitivity to weak lattice distortions is much higher than that of other X-ray methods. This review describes the physical foundations and implementation of the section topography techniques, as well as the results of computer simulating the wave field in a crystal. We present some examples of solving materials science and microelectronics problems and briefly describe the section topography using synchrotron radiation.

Keywords: X-ray topography, single crystals, defects in crystals, silicon, diamond, indium antimonide.

DOI: 10.21883/TP.2022.10.54354.23-22

Introduction

Section methods occupy a special place in X-ray diffraction topography, since they allow one to obtain quantitative information about local deformations of the crystal lattice caused by defects. They make it possible to study the structure of the X-ray wave field formed inside the lattice scattering triangle near the Bragg reflection. In turn, the analysis of the structure of the wave field in the scattering triangle reveals information about local deformations associated with the crystal lattice defects. High sensitivity to local deformations is based on the analysis of the geometry of the Kato interference fringes formed on section topograms in the scattering triangle. The X-ray wave field arising in a crystal lattice near the Bragg position is described in detail by the dynamic scattering theory. This is the theoretical basis of X-ray section topography. Essentially, section topography is a single-crystal X-ray interferometer method. (The Kato fringes are the result of the interference of normal and anomalous waves.)

Section methods of X-ray topography (XT) are implemented in two geometries — diffraction according to Laue and according to Bragg. In the second case, due to the features of the wave field reflection by the crystal surface, it is difficult to observe the Kato fringes. However, even a slight bending of a crystal with a radius of curvature of hundreds of meters leads to the formation of another type of interference fringes, the geometry of which makes it possible to determine very weak deformations.

Section XT is used to study various defects of the crystal lattice, their geometry and type of elastic fields; decomposition of solid solutions; impurities in doped crystals; impurity gettering effects; detection of defects with weak deformation fields, which are insufficient for the formation of a direct (kinematic) image, etc. In this review, we consider the possibilities of section XT methods usage to study the actual structure of crystals.

1. Physics of section methods

The idea of X-ray diffraction topography was first formulated in 1931 in the papers of V. Berg [1,2]. During the following years many different XT schemes were developed (the schemes of Berg–Barrett, Schulz, Fujiwara, Bormann, etc.), but most of them only made it possible to visualize large defects and grain boundaries and to reveal the geometric and spatial position of defects in a crystal.

In 1954 A.R. Lang [3] proposed and published a fundamentally new scheme (Fig. 1) of XT, on the basis of which modern quantitative methods of X-ray diffraction topography were created, which make it possible to measure local deformations associated with the crystal lattice defects. In Lang's original scheme (Fig. 1) a narrow X-ray beam is incident on the crystal from a „point source"formed by a narrow slit, so that the crystal singles out only one characteristic line of the spectrum from the entire white spectrum, for example, K_α. With the help of a special goniometer the crystal is placed in a reflective position for some system of planes (hkl). The scheme provides for one more collimator, which makes it possible to single out a diffracted or passing beam for subsequent registration. In Lang's geometry three options for obtaining images are possible: topograms with scanning, when a diffraction image of the entire crystal is recorded in diffracted or passing beams due to the continuous movement of the crystal and detector under the X-ray beam; limited topograms, when only the part of the diffracted or passing beam singled out by the second collimator is recorded (this makes it possible to

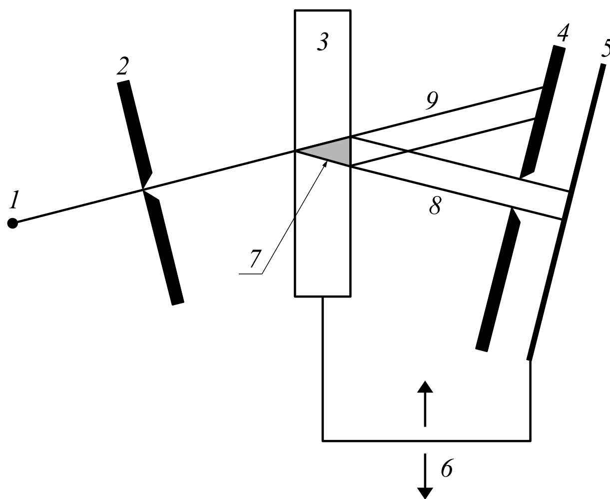

Figure 1. X-ray optical scheme of the Lang method: *1* — point source of X-rays; *2* — slit forming the X-ray beam; *3* — crystal under study; *4* — slit separating the beams diffracted (*8*) or passed through the crystal in the direction of the incident X-ray wave (*9*); *5* — detector registering a topogram; *6* — scanning mechanism; *7* — scattering triangle.

obtain information about the depth of defects in the crystal) and, finally, section topograms, when scanning is stopped and a stop-frame is recorded, i.e., the image formed at the base of the scattering triangle on the exit surface of the crystal. Such topograms fundamentally differ from all others by the possibility of obtaining quantitative information about local distortions of the crystal lattice due to defects.

1.1. Conditions for implementing section methods

For the practical implementation of section topography, a point source of a divergent X-ray wave on the crystal surface is required. The point source can be obtained in two ways:

a) a narrow slit is placed in front of the crystal;

b) the incident wave is focused on the crystal surface by a special X-ray optical device.

In section topography on a laboratory source the narrow slit in front of the crystal is a secondary source of X-ray radiation. It should be located as close to the crystal as possible. The parameters of the secondary source determine the geometric resolution of the method and depend on the focus and distance to the primary source and its spectrum. The second option of the secondary point source obtained by focusing is possible only on a synchrotron source [4].

The section methods implementation in the spherical wave approximation in practice means the collimation of the incident beam. The width of the slit in front of the crystal must be much smaller than the width of the base of the scattering triangle, $a \ll 2t\,\mathrm{tg}\,\theta_{\mathrm{B}}$, where t is the crystal thickness, and θ_{B} is the Bragg angle of reflection used. Usually, the a order parameter is $\lambda\,\mathrm{tg}\,\theta_{\mathrm{B}}$, where λ is the extinction length. For a silicon crystal and $\mathrm{Mo}K_{\alpha 1}$ radiation, this is about $10\,\mu$m in the reflection (220) and $15-20\,\mu$m in the reflection (440).

Note that various modifications of Lang's section method in which these conditions are not met (for example, when using laboratory radiation sources they include the stop-frame method, the method of limited projections, etc.) are not considered in this review [5].

The degree of absorption of X-rays is of particular importance. The Kato interference fringes are clearly observed only at low absorption $\mu t/\cos\theta_{\mathrm{B}} < 3$ (when both waves, i.e., normal and anomalous, reach the base of the scattering triangle) and only in perfect crystals. Here μ is the photoelectric absorption coefficient [6]. Therefore, when using laboratory sources of radiation by section methods the crystals of silicon, diamond, silicon carbide, and quartz were mainly studied. It was possible to expand this list by using synchrotron radiation. Note that if section methods are used only to estimate the defects position through the crystals thickness, the limitations on X-ray absorption are not fundamental.

In the crystal located near the exact Bragg reflection, a region limited by the directions of the wave vectors of the incident K_0 and diffracted K_{H} waves of the scattering triangle is illuminated. According to the dynamic scattering theory the wave field in this triangle is formed as a result of the interaction (interference) of normal and anomalous waves arising from the splitting of the dispersion surface in the vicinity of the exact Bragg position (at the boundary of the Brillouin zone). The form of such wave fields is shown in Fig. 2 [7,8]. This is an analytical calculation of the wave field inside the crystal, obtained by solving the Takagi–Topen equations [9–13].

On section topograms (at the base of the scattering triangle on the exit surface of the crystal) these wave field oscillations lead to the formation of intensity interference fringes. In literature these fringes are called the Kato fringes [14]. Fig. 3 shows typical experimental section topograms of the ideal crystal ($\mu t < 1$) [15].

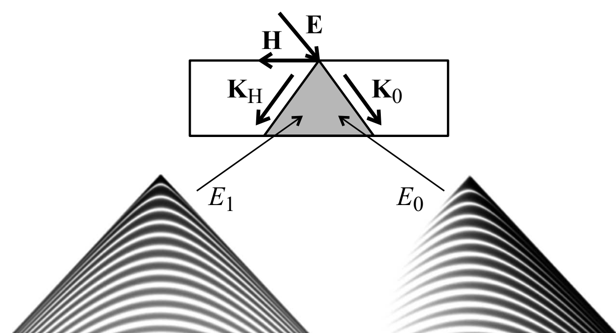

Figure 2. Analytical calculation of the amplitude of the diffracted and passing waves in the scattering triangle. $\mathbf{K}_0$ and $\mathbf{K}_H$ are wave vectors of the incident and diffracted waves, H is the diffraction vector (vector of reciprocal lattice) perpendicular to the reflecting planes (hkl) [7,8].

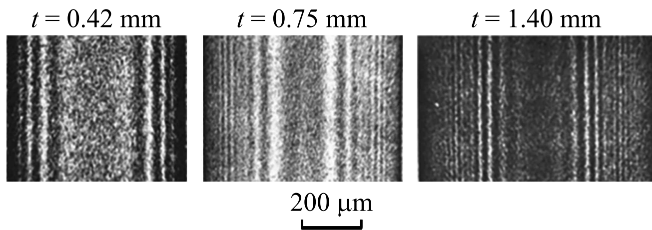

Figure 3. Experimental section topograms of defect-free silicon single crystals of various thicknesses obtained in a diffracted beam. Mo$K_{\alpha 1}$ radiation, reflection plane (224) is perpendicular to the crystal surface, t — crystal thickness [15].

1.2. Methods for describing and modeling the wave field in a crystal

The interaction of X-ray radiation with crystal lattice is a complex physical process that manifests itself in the form of numerous diffraction effects. The propagation of X-ray wave field in crystal lattice is described by the dynamic scattering theory developed by P. Ewald and M. Laue (1926−1931). This theory is based on the analysis of dispersion relations obtained by solving the wave equation of Maxwell's electromagnetic theory. In the two-wave approximation (only the incident and one diffracted waves are considered in the experiment) the dispersion surface in the vicinity of the Bragg reflection is splitted into two sheets, which are described by a system of two dispersion equations. The analysis of these relations is quite clear and is used to study and describe wave fields in ideal crystals. Another approach was developed much later by S. Takagi [9,10] in Japan, by D. Topen [11,12] in France, by A.M. Afanasiev and V.G. Kon [16] in Russia. The direction developed by S. Takagi and D. Topen turned out to be universal, since it makes it possible to study not only ideal crystals, but also crystals with local distortions of the crystal lattice. This approach is based on solving a system of differential equations describing the propagation of a self-consistent wave field in the crystal lattice that has local distortions associated with defects. These equations are called the Takagi−Topen equations.

In the two-wave approximation, when two strong waves, i.e., passing and reflected, propagate in the crystal, the system of equations has the form:

$$\begin{cases} \frac{\partial E_0}{\partial s_0} = -i\pi K C \chi_{-H} E_H \\ \frac{\partial E_H}{\partial s_H} = -i\pi K C \chi_H E_0 + i2\pi K \beta_H E_H \end{cases}. \quad (1)$$

Here E_0 and E_H are the amplitudes of the passed and diffracted waves; $K = 1/\lambda$; χ_H, χ_{-H} are Fourier components of the crystal polarizability for the reciprocal lattice vectors $\mathbf{H}$, $-\mathbf{H}$, respectively; s_0 and s_H are coordinates along the directions of the transmitted and reflected waves; C are polarization factor equal to one, and $|\cos 2\theta_B|$ for σ and π — polarization. The function β_H describes the local deviation of the reflected wave from the exact Bragg angle θ_B and is related to the displacement field inside the crystal $\mathbf{u}(x, y)$ by the relation

$$\beta_H = -\Delta\theta \sin\theta_B - \frac{1}{K}\frac{\partial(\mathbf{Hu})}{\partial s_H}, \quad (2)$$

where $\Delta\theta$ is the angular deviation of the incident wave from the exact Bragg angle.

The applicability condition for the Takagi differential equations system: the amplitude of waves in a crystal is a slowly varying function at a characteristic distance $L = \sqrt{\lambda\Lambda}$, where $\Lambda = \lambda \cos\theta_B / C\mathrm{Re}\chi_H$ is the Laue pe-extinction length [10,17].

In the X-ray wavelength range this characteristic distance is about $0.05\,\mu$m, which is much less than the resolution of the XT method, which is rarely better than $\sim 1\,\mu$m, because it is limited either by the detector resolution, or by point scattering function in diffraction topographic imaging. Consequently, the Takagi equations describe the dynamic X-ray diffraction in crystals with practically any kind of defects.

In the case of an ideal crystal and point source on the crystal surface, the solution of system (1) corresponds to the Kato theory of spherical waves. Then the radiation in the crystal propagates only inside the scattering triangle, limited by the refracted and reflected rays. In the transmission geometry (Laue geometry) with symmetric diffraction the intensity of the reflected wave in the crystal is described by the expression (3) [18,19]:

$$I_H(x) = P \left| J_0 \left(\pi z (1 + i\delta) \sqrt{1 - s^2} / \Lambda \right) \right|^2. \quad (3)$$

The condition $0 < z < t$ corresponds to the crystal region, and the coordinate x is measured from the point O on the input surface of the crystal, for which the Bragg equation is exactly satisfied. $J_n(\xi)$ are the Bessel cylindrical functions of n-order; $\delta = \mathrm{Im}(\chi_H)/\mathrm{Re}(\chi_H)$, $s = x/(z\,\mathrm{tg}\,\theta_B)$ is the dimensionless parameter changing within the energy flow of triangle from -1 to 1. Normal absorption is described by the parameter $P = \exp(-\mu z/\cos\theta_B)$, where μ is the linear photoelectric absorption coefficient. The intensity distribution of the reflected wave observed at the exit surface of the crystal at low absorption ($\mu t < 3$) has an aperiodic oscillating nature with pronounced edges. In the center of the image there are slow oscillations. Towards the edges of the image the frequency of oscillations increases with the amplitude increasing up to P^2. This pattern is well known in section topography as the pendulum Kato fringes in spherical X-ray wave diffraction.

In Bragg geometry the situation is different. The intensity of the scattered wave on the crystal surface is described by the formula (4) [16,20].

$$I_H(x) = P|J_0(\pi x(1 + i\delta)/\Lambda) + J_2(\pi x(1 + i\delta)/\Lambda)|^2, \quad (4)$$

where the x coordinate is measured along the crystal surface, $P = \exp(-\mu x/\cos\theta_B)$. The intensity distribution described by expression (4) has a main maximum with amplitude 1, the width at half the height equal to 0.5Λ, and

a first minimum at a distance of 1.25Λ. Lateral maxima are located only on the right side and rapidly decrease in amplitude. Thus, the intensities of the first three lateral maxima with respect to the main maximum are 1.5, 0.3, and 0.1%, respectively. The matter is that the functions $J_0(\chi)$ and $J_2(\chi)$ differ significantly only in the region of the first oscillations. Experimental observation of these fringes is possible only with significant overexposure of the image [20,21], as well as in the case of asymmetric reflection [22]. At present, some authors call these fringes „the Uragami fringes".

An exact analytical solution to the Takagi equations system with an arbitrary displacements field cannot be obtained. The exception is the crystal with a constant deformation gradient [23]. The solutions are quite complex and can only be analyzed in their asymptotic form. Therefore, the theory of diffraction contrast develops in two directions. The first approach is associated with approximate methods for solving the system of equations and with the qualitative analysis of the main image details. In is way, the method of dominant functions and the method of geometrical optics are effective methods for image interpreting [7]. The second approach is associated with the use of numerical mathematical methods for solving equations for defects of various types and arbitrary form of the front of the incident X-ray wave.

1.3. Section method in Laue geometry

In the crystal lattice local deformation fields associated with defects will affect the nature of the trajectories of normal and anomalous waves in the scattering triangle. As a result, the interference fringes will shift, and new interference fringes will appear. The analysis of the resulting interference pattern makes it possible to obtain quantitative information about the parameters of the deformation field associated with the defect. This idea was first practically realized in N. Kato paper [14]. Fig. 4 shows the results of this experiment. A crystal was used in the form of a silicon plate, on one side covered with oxide film. A window is etched in the film (Fig. 4, *a*), and a section topogram is taken at the edge of the oxide film (Fig. 4, *b*). The image clearly shows how the interference fringes (Kato fringes) are displaced near the edge of the film, where local deformations of the near-surface layer of the crystal are formed. The displacement of the fringes can be used to determine the magnitude of local deformations. Due to large local deformations a bright spot appears at the edge of the oxide film, which is caused by the scattering of a wide spectrum of waves $\Delta\lambda$ (not only $K_{\alpha 1}$, on which section topogram is formed) and is called as direct or kinematic image.

Most quantitative methods of X-ray diffraction topography are based on the analysis of the displacements of such interference fringes in section topograms. This makes it possible to determine the parameters of local deformation fields associated with defects in the crystal lattice.

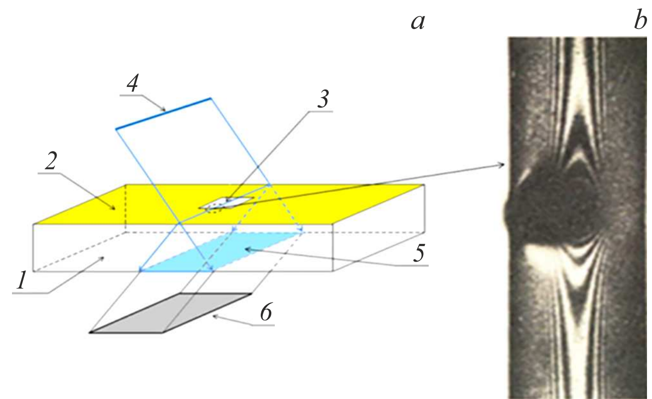

Figure 4. Section topography at the edge of the oxide film, silicon single crystal. *a* — experimental scheme: *1* — crystal under study, *2* — oxide film, *3* — etched window in the oxide film, it4 — incident X-ray beam, *5* — base of scattering triangle, *6* — detector registering the diffracted beam. *b* — experimental section topogram, Mo$K_{\alpha 1}$ radiation, the region of the crystal displayed on the section topogram is outlined in the scheme by a dotted line [14].

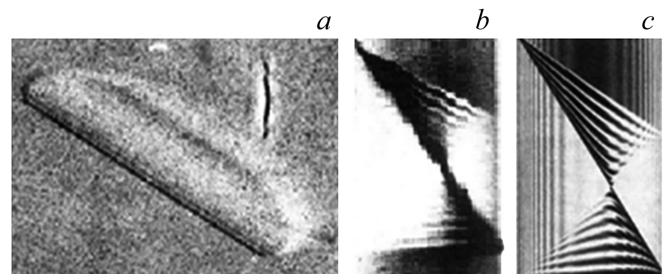

Figure 5. X-ray topograms with stacking fault image: *a* — projection X-ray topogram of stacking fault in a silicon single crystal. Radiation CuK_α, reflection plane (111); *b* — experimental section topogram with stacking fault; *c* — numerical simulation of stacking fault image on a section topogram [24].

In 1975 A. Autier published interesting studies of stacking faults in single crystals of silicon using section topography methods. Fig. 5 shows some of these results [24]. Note that the interference fringes on the section topogram in the vicinity of the stacking fault do not shift and bend, and this confirms the absence of local deformations associated with stacking faults. In the described experiment the stacking fault is located obliquely to the system of reflecting planes. Section topograms show two triangular regions with new interference fringes touching the vertices. Such a contrast arises due to the formation of interbranch scattering on the stacking fault plane. On one and the other sides of the plane in two scattering triangles the two wave fields are formed, i.e., normal and anomalous, the interference between which forms the contrast observed in Fig. 5.

The first systematic studies of the diffraction image of defects in section topography (on the example of dislocations) were started by a team headed by prof. A. Autier [25,26].

Fig. 6 shows diffraction images of D dislocation located obliquely in a silicon single crystal, which has the form of a rectangular prism with a thickness of 0.8 mm. Radiation $MoK_{\alpha 1}$ reflecting planes (220), $\mu t = 1.12$. The analysis of the experimental section topograms and the results of numerical simulation showed that the obtained dislocation images have a complex structure. It consists of at least three components of different physical nature. According to A. Autier terminology the part of the image marked as i_1 was named „direct or kinematic image". The contrast is formed as a result of the scattering of a wide spectrum of X-ray wave in a strongly distorted region near the dislocation core. The light part of the contrast i_2 (light shadow), „dynamic image", is the result of transferring a part of the wave field energy to the direct image. The oscillating part of the contrast i_3, „intermediate image", is formed as a result of the interference of the main wave field in the scattering triangle and interbranch scattering waves generated by scattering on elastic distortions of the dislocation field [13,27,28]. The Kato fringes are weakly traced in the experimental topogram, which is apparently due to the low linear resolution of the experiment.

The analysis of section images of dislocations shows that the contrast for each particular geometry of the dislocation position in the scattering triangle is formed due to different diffraction mechanisms. Therefore, to simplify the analysis of these mechanisms operation, it is more convenient to use straight dislocations. As a rule, growth dislocations in single crystals have a complex structure and shape, which significantly complicates the analysis of section topograms. A method for preparing silicon samples with linear single dislocations (screw and 60°-degree) was developed at the Institute of Solid State Physics of the Academy of Sciences of the USSR under the management of V.I. Nikitenko [29].

Consider the geometry in which the dislocation axis is oriented along the diffraction vector. Fig. 7 shows three section topograms with dislocations in this geometry [30,31]. For each topogram the numerical simulation of the dislocation image and the wave field type in the scattering triangle was carried out. The analysis of the obtained images by the displacement of the interference fringes makes it possible to determine the magnitude of the

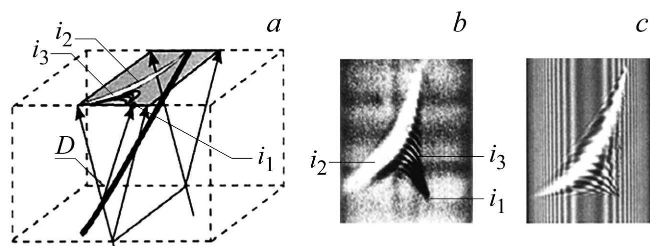

Figure 6. a — schematic representation of crystal with tilted dislocation D; i_1 — direct image of dislocation, i_2 — dynamic image, i_3 — intermediate image; b — experimental section topogram; c — result of numerical simulation of section topogram by solving the Takagi–Topen equations [28].

Burgers vector $b = 3.79 \pm 0.39$ Å. For silicon single crystals this value is in good agreement with the literature data. The topogram (Fig. 7, b) shows 60°-degree single dislocation. The screw component of the Burgers vector, directed along the diffraction vector and causing the main distortions of the reflecting planes, is only half of its modulus and practically does not cause the Kato fringes displacement. Two other topograms (Fig. 7, c, d) demonstrate noticeable displacements of the fringes, and these displacements can be used to determine the magnitude and type of local deformations of the reflecting planes. Numerical simulation of the wave field inside the scattering triangle (Fig. 7, e) shows that the local elastic field of dislocations leads to the wave field focusing and the direct image formation.

In the papers of E.V. Suvorov, I.A. Smirnova, E.V. Shulakov another type of dislocation orientation in the scattering triangle is given i.e., when the dislocation axis is simultaneously perpendicular to the diffraction vector and the input surface of the crystal [32]. Figure 8 shows the scheme of the experiment (Fig. 8, a), experimental section topograms (Fig. 8, b; *1*), corresponding results of numerical simulation of topograms (Fig. 8, b; *2*) and the nature of the wave field in the scattering triangle (Fig. 8, b; *3*). Two cases are considered: when the dislocation axis crosses the incident beam near the edge of the scattering triangle (D_1), and when the dislocation axis is located along the vertical bisector of the scattering triangle (D_2).

The analysis of section topograms and the results of numerical simulation makes it possible to understand how the image of dislocations is formed in this geometry. The deformation field of the dislocation D_1 inside the scattering triangle forms a new interbranch scattering field. As a result of this field interference with the already existing one, a new small scattering triangle arises, the intense part of which creates a direct image with a light shadow. For the dislocation D_2 located along the bisector of the „scattering triangle", just as in the first case, the interbranch scattering field is formed, the interference of which with the existing field leads to the effect of wave channeling along the dislocation axis. The light wings to the right and left of the dislocation axis are the result of the transfer of the main fraction of the field energy to the channel on the dislocation axis.

To ensure complete information on the formation of the diffraction contrast of dislocations, another geometry of dislocation position in the scattering triangle is of interest, when the dislocation axis is parallel to the reflecting planes (perpendicular to the diffraction vector) and perpendicular to the scattering plane. Fig. 9 shows the results of the study of this geometry [33]. Two positions of the dislocation axis are considered — the dislocation is located outside the scattering triangle (position D_1), and the dislocation intersects the scattering triangle (position D_2) near the vector $\mathbf{K}_0$.

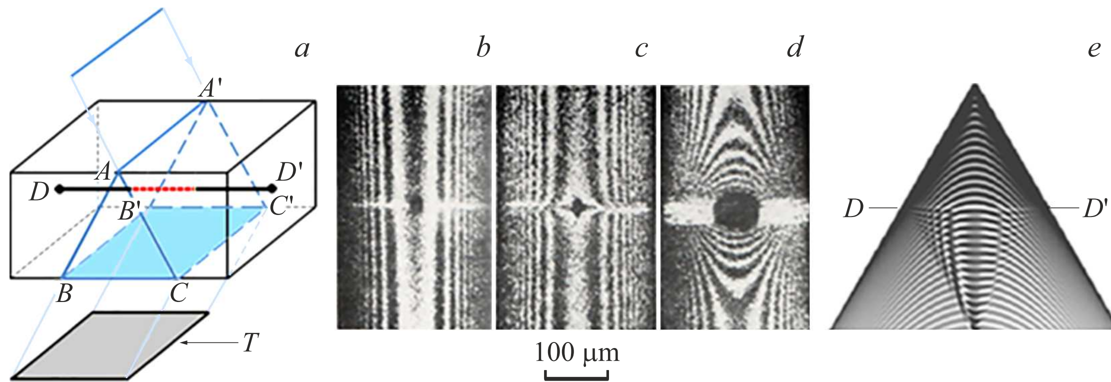

Figure 7. Section topograms of screw and 60-degree dislocations in a single crystal of silicon: a — scheme for obtaining a section topogram (DD' — dislocation axis, its red dotted part (in the online version) passes inside the scattering triangle, T — topogram); b 60°-degree single dislocation; c — single screw dislocation; d — a group of 14 closely spaced screw dislocations; (e) — numerical simulation of the wave field in the scattering triangle for single screw dislocation. Mo$K_{\alpha 1}$ radiation, reflecting plane $(20\bar{2})$, sample thickness $t = 410\,\mu$m [30,31].

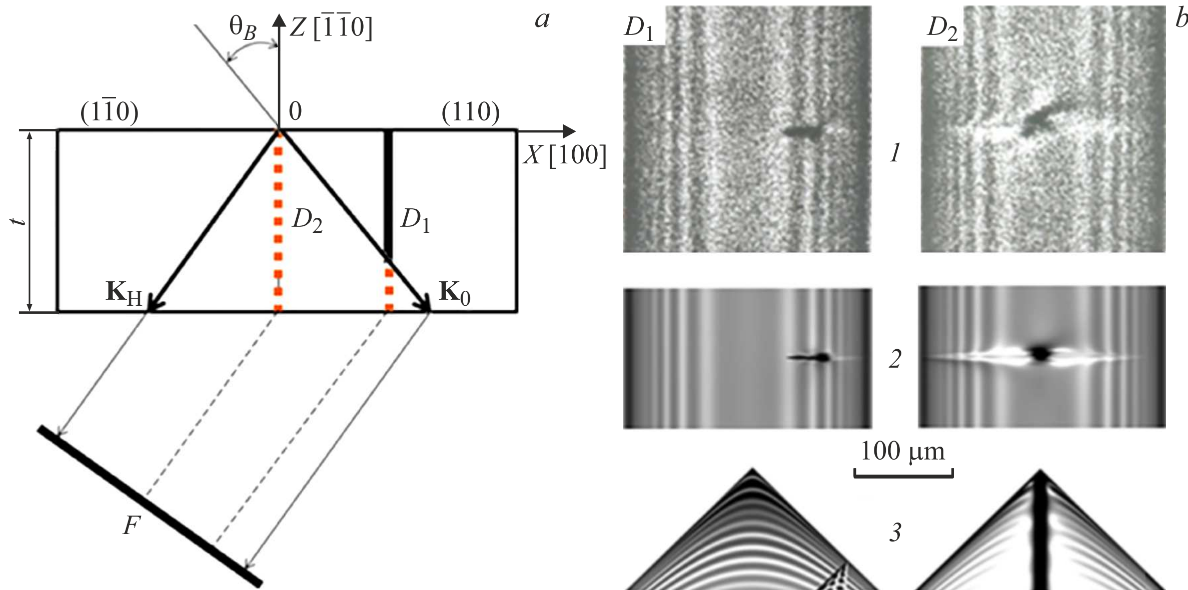

Figure 8. a — scheme of the experiment; b — results of the experiment. Section topograms (1); results of numerical simulation of section topograms (2) and wave field in the scattering triangle (3). D_1 and D_2 — positions of 60-degree dislocations in the scattering triangle. The red dotted line (in the online version) marks the dislocation regions located inside the scattering triangle. Silicon crystal thickness $t = 450\,\mu$m, Mo$K_{\alpha 1}$ radiation, reflection (004) [32].

Here, as in the previous examples, interbranch scattering waves are formed when the wave field of diffracted or passing wave interacts with the local elastic field of D_2 dislocation. As a result of these waves interference the maxima and minima of the total field are formed, which creates a complex diffraction contrast of dislocations.

1.4. Study of weakly distorted crystals by section methods

The high sensitivity of section topography to local deformations makes it possible to study rather weak distortions of the crystal lattice associated with various kinds of clusters, precipitation of impurities, etc. In papers [34–36] various macrodefects are investigated. Fig. 10 shows a fragment of section topogram of the silicon single crystal with an image of a macrodefect.

From the analysis of section topograms, it is possible to estimate the size of such defect: $\sim 0.25\,\mu$m. The defect does not give a direct image, which indicates a very small amount of local deformations. Apparently, the formation of such defects is associated with an uneven distribution of dispersed oxygen-containing precipitates.

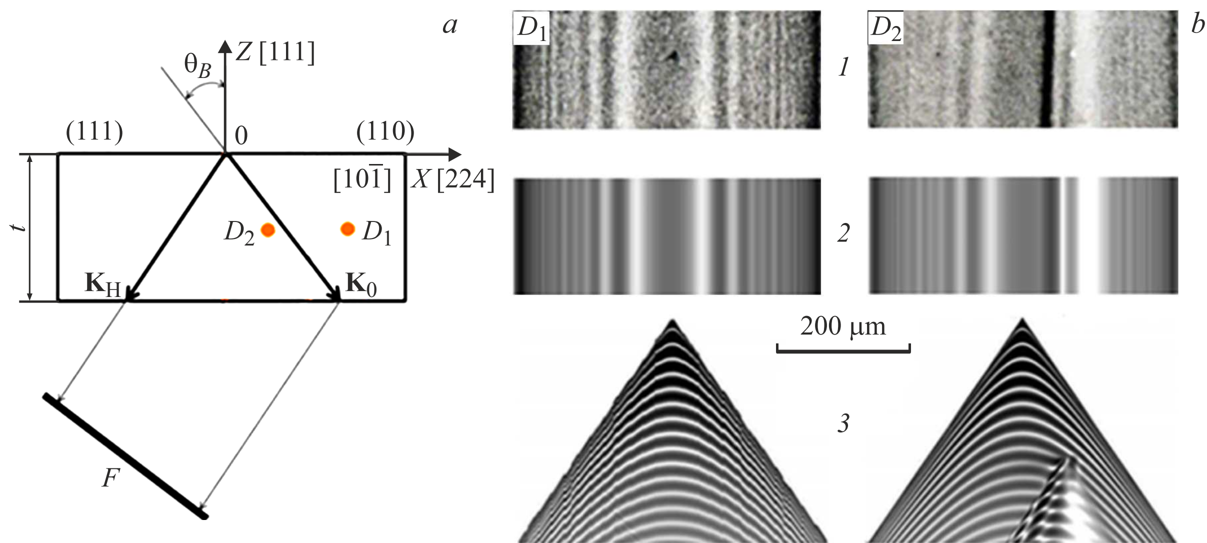

Figure 9. *a* — scheme of the experiment. Red dots D_1 and D_2 — traces of dislocations perpendicular to the Figure plane [10$\bar{1}$]; *b* — results of the experiment. *1* — experimental section topograms; *2* — results of numerical simulation — topograms; *3* — view of the wave field in the scattering triangle [33].

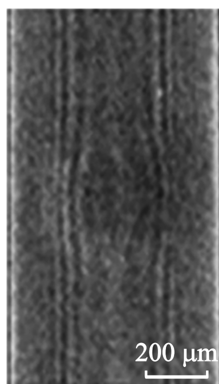

Figure 10. Fragment of section topogram of a silicon single crystal showing a macrodefect. Silicon single crystals are doped with phosphorus to a concentration of $1.1 \cdot 10^{20}\,\mathrm{cm}^{-3}$. Radiation Mo$K_\alpha$, reflection (440) [34].

The numerous examples considered above show that the local deformation fields of the crystal structure violate the normal pattern of the Kato interference fringes. However, keep in mind that there is another source of fringes distortion even in the absence of defects — this is multiple diffraction. If the angular size of the source along the fringe is small, then different sections of the topogram in this direction correspond to different values of the azimuthal angle. At some values the conditions of multiple diffraction are realized, and other reflected beams appear. The distortion of the fringes occurs due to a change in the nature of the radiation interaction with the crystal.

Such violation of interference fringes in multiwave section topography was studied in [37] using synchrotron radiation, but exact theoretical calculations were not carried out. In paper [38] an exact theoretical calculation was carried out for three cases of multiple diffraction revealed on one section topogram of the silicon crystal. The calculation results are in good agreement with the pattern of interference fringes obtained using the laboratory source.

1.5. Section method in Bragg geometry

Let us consider X-ray scattering on the ideal crystal plate in reflection geometry (Bragg geometry). Let us choose the origin of coordinates XZ at the point O on the input surface, where the Bragg condition is exactly satisfied (Fig. 11). The plate is limited by the side face BC. The radiation output through the side face makes it possible to experimentally study the intensity distribution of wave fields in the bulk of the sample. The amplitude of the scattered wave on the crystal surface is described by formula (4). The first term in (4) describes the scattering of the primary wave in the bulk of the crystal. The second term corresponds to the scattered wave specularly reflected from the input face of the crystal. The function $J_2(\pi x/\Lambda)$ differs significantly from the function $J_0(\pi x/\Lambda)$, taken with minus sign, only in the region $x/\Lambda < 1.5$. This means that the specularly reflected wave at $x/\Lambda > 1.5$ is shifted in phase relative to the primary one by π. This behavior of the specularly reflected wave leads to the fact that the resulting amplitude of the scattered wave on the crystal surface, near the point of radiation entry into the sample, has a bright burst of intensity with an amplitude of 100% (main maximum) and width at half-height equal to 0.5Λ. The first minimum is located at a distance of 1.25Λ. Other maxima are located only on the right side and rapidly decrease in amplitude. As a result,

in the region $x/\Lambda \gg 1.5$ we have a zero amplitude of the scattered wave under conditions when the amplitudes of the bulk and specular reflected waves differ significantly from zero. Any defect introduction into this region changes the phase relationship between the waves of the first and second types, and the defect image becomes clearly visible [39].

Fig. 11, *b* shows the intensity distribution of the diffracted wave field in the OBC volume for unpolarized radiation. It can be seen that the main contribution to the intensity of scattered waves is concentrated along the trace of the passing beam. Near the surface the intensity has a significant value only in the vicinity of the point O. As the observation is shifted deeper into the crystal, the intensity of the scattered waves increases. The oscillatory nature of the intensity distribution in the energy flow triangle OBC is associated with the pendulum effect during dynamic X-ray scattering in perfect crystals. Thus, the role of the specular wave comes down not to interference with the main wave, but only to change in the total amplitude of the scattered wave. These changes are large in the near-surface layer of the crystal, in which the total intensity of the scattered waves is completely extinguished, and decrease as the observation is shifted deeper into the crystal.

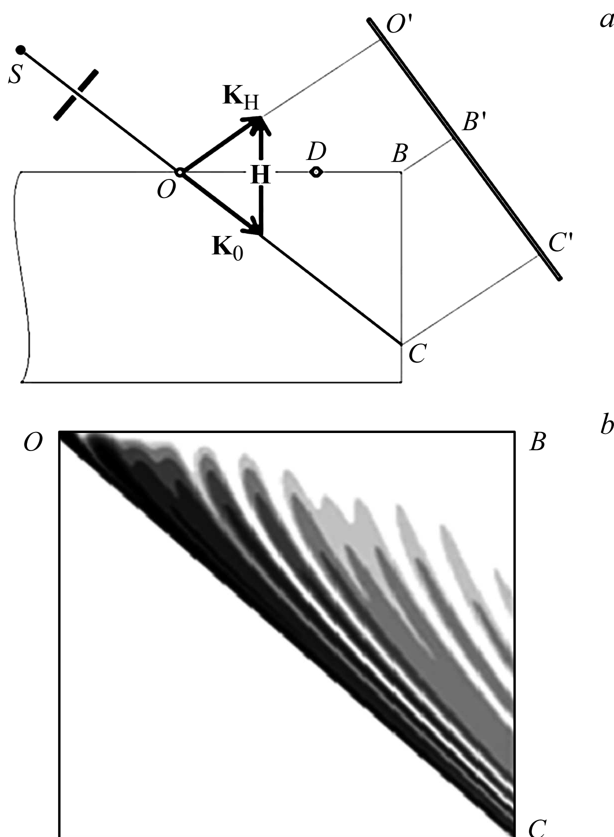

Figure 11. Scheme of the experiment: *a* — a point *D* on the crystal surface corresponds to a quasi-point defect caused by a puncture with an indenter; *b* — numerical simulation of the wave field pattern in the bulk of the crystal was performed for the case of an ideal crystal [39].

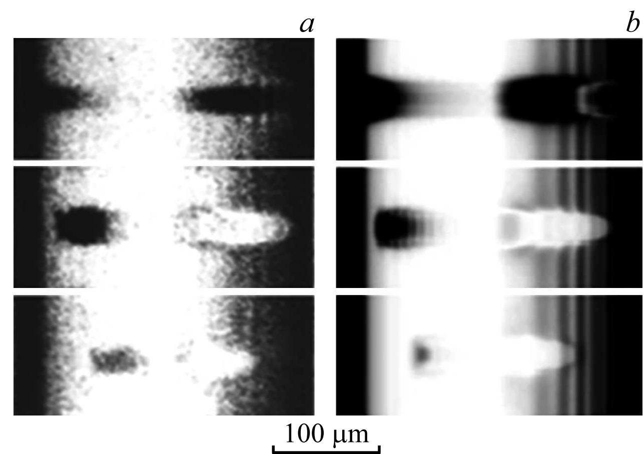

Figure 12. Experimental section topograms (*a*) and numerical simulation of images of silicon crystals (*b*) with defects deposited on the input face. The distance to the defect OD in the Figures from top to bottom is 15, 165 and 315 μm [39].

Fig. 12, *a* shows the experimental topograms of three defects located at different distances from the point O. The left half of the topogram corresponds to the intensity distribution on the segment OB, the right — on BC. At both edges of the image the intensity oscillations are observed: on the left — intensity oscillations during the Bragg diffraction (Uragami fringles), on the right — in the sample bulk. In the center of each fragment images of defects are visible — bright paired images. Defects correspond to the damage of the crystal surface by a Vickers pyramid with a load of 1 to 6 g at distances of 10 to 400 μm from point O. The image of defects depends on their position relative to the point O. On the upper fragment the defect is located in the region $x < \tau/3$, and the image of the defect is formed only by the wave field $J_0(x)$ only. Images of the defect in both halves of the topogram are formed in the usual way. The defect image consists of a kinematic part — a local burst of intensity — and a dynamic „tail"trailing after the burst. The rest of the defects are separated from the region of the intense Bragg reflection and are located in the zone with almost zero intensity of the scattered beam. At the same time, they give a bright contrast image on the topogram. The topographic contrast of the images of these defects is related to the phase mismatch in the region of the defect between the reference wave scattered in the perfect bulk of the crystal and the object wave reflected from the input surface of the sample. The results is that the object wave no longer suppresses the reference wave. This is an unique type of „phase contrast".

The paper [40] describes a fundamentally different type of interference fringes in Bragg geometry, associated with the crystal lattice bending and called deformation interference fringes. This phenomenon was studied experimentally on crystals with amorphous oxide film, and the mechanism of deformation fringes formation [41–43] was described using geometric X-ray optics. The features of the formation of

interference defect fringes on uniformly bent crystals are studied by the methods of section topography and numerical simulation in Bragg geometry. The role of interbranch scattering in the formation of defect fringes (bending contours) in a bent lattice was studied. The possibility of using „bending interference contours" for measuring very weak surface deformations caused by quasi-point defects is shown. It was founded that the differences in the intensity of the fringes for the positive and negative signs of the bending gradient are associated with the difference in the focusing of normal and anomalous waves.

To perform experiments on bent crystals, a special goniometric device was used for precision bending of the crystal with bending radii in the range of about $10-300$ m (the crystal deflection for this range of bending radii is approximately $50-300\,\mu$ m) [44]. As a result of numerous

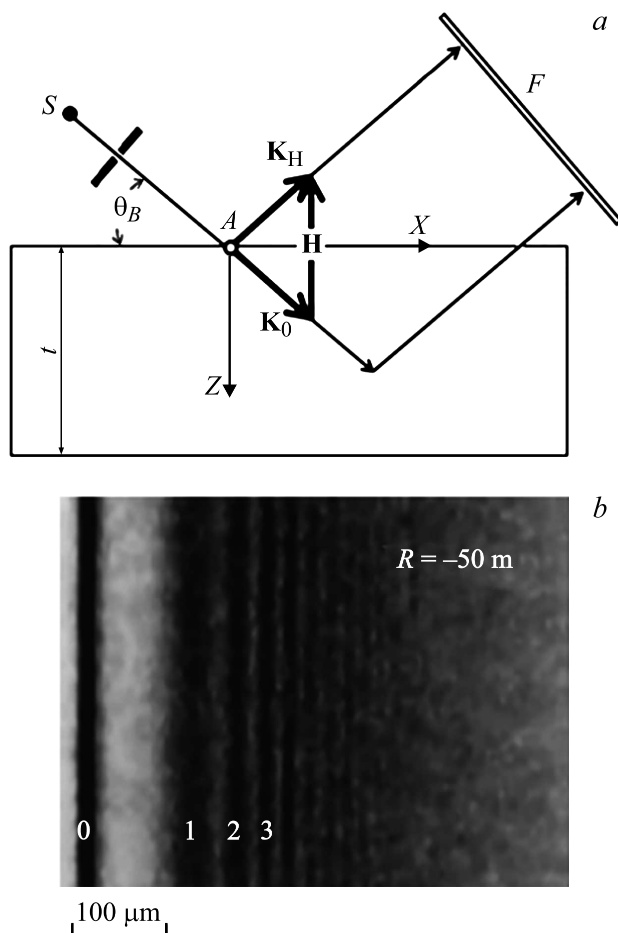

Figure 13. Scheme of experiment and section topogram with deformation fringes: a — scheme of experiment: $\mathbf{K}_0$, $\mathbf{K}_H$ — wave vectors of the incident and diffracted waves, $\mathbf{H}$ — diffraction vector, F — detector, S — collimator, θ_B — Bragg angle, b — section topogram of a silicon single crystal, obtained in Bragg geometry (numbers on the topogram are numbers of the first three bending contours; bending radius: -50 m; sign minus corresponds to the deformation gradient decreasing along the axis Z; the bright line with index 0 corresponds to the edge of the topogram.) The topogram was obtained in Mo$K_{\alpha1}$ radiation [44].

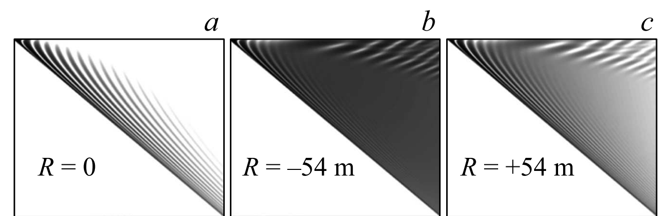

Figure 14. The intensity distribution of the wave field in the scattering triangle in Bragg geometry. Reflections Si(004), radiation Mo$K_{\alpha1}$, the Bragg angle is $15.141°$; height of each image $900\,\mu$m, width $3326\,\mu$m; a — ideal crystal, bending radius $R = 0$; b — bent crystal, the bending radius is $R = -54$ m; c — bending radius $R = +54$ m [45].

experiments and numerical simulations, it was established that the bending contours are formed as a result of the interference of reflected wave and interbranch scattering waves, which are generated due to the deformation gradient directed along the bending radius of the crystal, i.e., along the diffraction vector. Fig. 13 shows the scheme of the experiment and the example of an experimental topogram. In the section topogram in Bragg geometry along with the usual interference contours, which are located on the left edge of the topogram in Fig. 13, b and merge into one bright line with index 0, the bending contours $(1, 2, 3$ etc.) are formed.

Numerical simulation of the X-ray wave field (solution of the Takagi–Topen equations) makes it possible to see the geometry of the wave field formation on the crystal surface and to understand the mechanism of the section topogram formation. Fig. 14 shows the wave fields in the ideal crystal, in the crystal with bending $R = -54$ and $+54$ m [45] of the first and second types

Ordinary interference fringes in Bragg geometry decay rapidly and are practically invisible in the experimental topogram (Fig. 13). When the crystal bending radius decreases the „fringes" shift towards smaller distances from the Bragg maximum. On the contrary, the bending radius increasing leads to the interference fringes shift away from the Bragg maximum. In this case their brightness decreases, and the fringes gradually merge with the background (at bending radii greater than 500 m). The unusually high sensitivity of bending interference contours to local deformations makes them extremely attractive for studying weak local surface deformations [46]. Fig. 15 shows the image of the quasi-point defect in the uniformly bent crystal.

The defect image consists of a kinematic intensity burst in the form of a black spot to the right of the Bragg maximum and a white trace perpendicular to the interference fringes. The experimental and calculated topograms demonstrate the displacement and bending of the contours in the deformation field of the defect. Estimates of the displacement of the first interference fringe near the defect correspond to the local bending radius of the reflecting

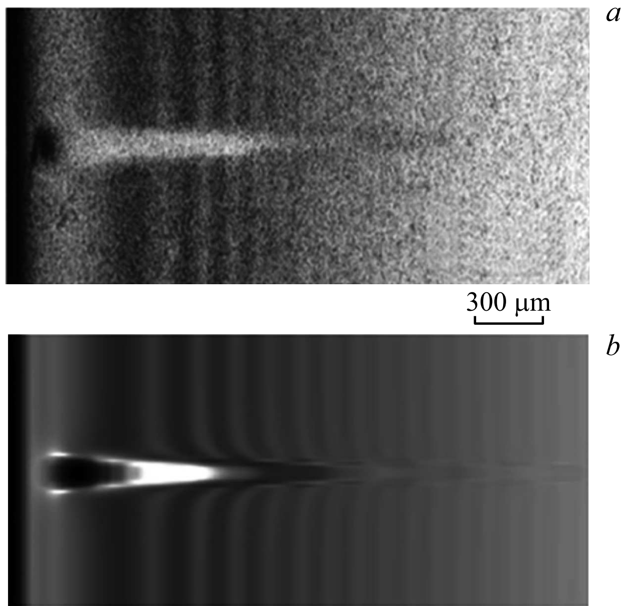

Figure 15. Section topograms of the silicon single crystal with a quasi-point defect on the surface: *a* — fragment of experimental section topogram, silicon single crystal, Bragg reflection (400), radiation Mo$K_{\alpha 1}$, crystal bending radius 150 m, the distance from the defect to the trace of the Bragg reflected beam $x = 190\,\mu$m; *b* — the corresponding numerical topogram obtained by solving the Takagi–Topen equations [46].

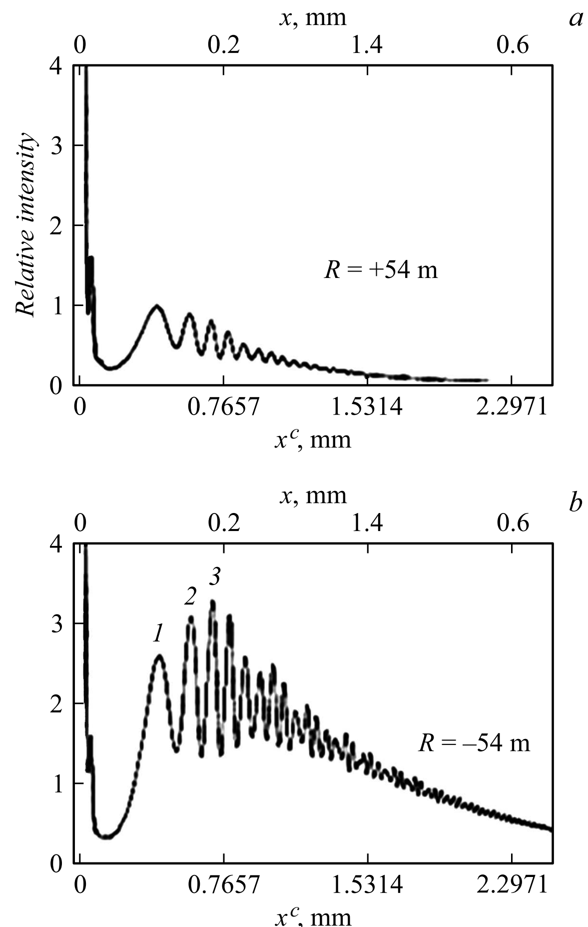

Figure 16. Simulation of the intensity distribution of deformation contours on the exit surface of the crystal. Unpolarized radiation. x — coordinate in the registration plane, x^c — along the crystal surface $x = x^c \sin\theta$ B [45].

plane $R \approx 540$ m [39,46]. The quasi-point defects were created by puncture by a Vickers indenter at loads of 1 to 5 g. In this model, it is assumed that the displacements under the surface of the sample are radial with respect to the contact point, and the surfaces of equal deformations have a hemispherical shape. The size of the hemispherical core was estimated based on the Vickers microhardness. For example, at a load of 5 g the core radius was $1.45\,\mu$m and agreed well with optical measurements. The example given shows that this method can be used to measure very slight surface deformations.

From experiments it was found that when the sign of the crystal bending changes, the brightness of the deformation fringes changes strongly. Comparison of Fig. 16, *a* and *b* also clearly shows that at positive bending radius the contrast of deformation fringes is much lower [45].

The analysis of this interesting phenomenon shows that it can be associated with the features of the trajectories spreading of normal and anomalous waves. It is known that interbranch scattering waves generated due to the deformation gradient in the bent crystal have significantly different absorption coefficients. In addition to this effect, there is also focusing [7,47]. As a result, at a positive bend the anomalous waves are focused, i.e,. are concentrated, and at a negative bend, they are defocused (weakened). Fig. 16 shows the result of numerical simulation of this process.

2. Solution of applied problems based on section topography methods

2.1. Study of nearly perfect crystals

With the help of section methods almost perfect crystals are effectively studied. Two types of problems are solved: the study of individual defects and the perfection assessment of the crystals structure as a whole. The possibilities of the methods in the study of individual dislocations and stacking faults are described in the first part of the review. Examples of characteristic images of screw, 60°-degree, and edge single dislocations of straight form at their different orientation in the scattering triangle, as well as a group of 14 closely spaced screw dislocations, are given. The analysis of the interference fringes in the vicinity of the dislocation images made it possible to determine the magnitude of their Burgers vectors. The calculation of section images and check of models of dislocation loops are known, as well as inclusions in the form of pores and precipitates of impurities [32,48,49]. Section images of defects differ

significantly from their images on projection topograms and require interpretation. However, they are so characteristic that they can be used to identify defects [50].

The second type of problems is associated with the perfection evaluation of crystals as a whole. They are solved on the basis of the interference fringes observation. With a distinct manifestation of fringes on the Lang section topograms, the deformation of the crystal lattice is less than 10^{-6}. Such crystals are considered perfect. In this case, the estimate refers to the bulk of the crystal, limited by the height of the topogram and its width. The topogram width is a scan of the crystal image through the thickness in the scattering triangle. If the topogram contains kinematic images of defects, then during its filming in symmetrical reflection and the film location perpendicular to the reflected beam at the near possible distance from the sample, it is possible to determine the position of defects through the crystal thickness based on a simple formula $x = (L/2) \times \sin\theta_{\mathrm{B}}$, where θ_{B} — Bragg angle, L — distance from the edge of the topogram, opposite to the direction of the diffraction vector, to the image of the defect. Due to the wide images of defects in this method the accuracy of such measurement is small, about 10%, but the method is non-destructive, and this is important for many problems. If it is necessary to assess the perfection of the structure of the large crystal, a series of section topograms is taken, moving the crystal after one topogram filming by a distance equal to its width. This method was tested with a synthetic diamond in the form of a thick plane-parallel plate $10 \times 10 \times 1.5\,\mathrm{mm}^3$ and proved to be an excellent method for assessing the structural perfection of crystals, which are a new material in physical materials science, necessary in the manufacture of X-ray optics elements, for example, synchrotron radiation monochromators. The feature of this paper is that with the help of a powerful laboratory source 18 kW a series of section topograms superimposed on the projection topogram was obtained from a diamond plate, and thus the structural perfection of the plate was assessed not locally, but as a whole (Fig. 17). The exposure to obtain one section topogram was half an hour, while when working with conventional radiation sources it would take several hours.

It is interesting to note that, according to the results of this method applying the synthetic diamond crystals containing microdefects were assessed as less perfect than crystals with dislocations. It can be seen that interference fringes are observed over a large extent of the section topograms, indicating a high structural perfection of most major portion of the plate bulk. These areas of the plate meet very high requirements during the X-ray optics manufacturing [51,52].

In addition to perfection assessment of the crystal structure as a whole on the basis of the interference fringes visibility, Fig. 17 makes it possible to observe how various defects affect the fringes, distort them, and even extinguish them in some places. Defect images can be used to determine whether they are surface or bulk: the width of the section topograms shows defects lying at different levels through the crystal thickness in the scattering triangle.

Figure 17. A series of section topograms superimposed on the Lang projection topogram of a synthetic CVD diamond plate $10 \times 10 \times 1.5\,\mathrm{mm}^3$. Ag$K_\alpha$-radiation, reflection 220.

At present, silicon remains the most perfect structure. But recently it was found that it also can have defects, even large ones. However, if they are characterized by a weak elastic field, then they can only be detected by the section method (Fig. 10), they are not detected by other methods. Dislocation-free silicon is still in demand in microelectronics, but interest gradually moves towards heavily doped silicon, which can contain many microdefects. Exactly this material is now the most actual for enhanced study and use. But it is characterized by the phenomenon of decomposition of solid solutions of impurities.

2.2. Investigation of the decomposition of solid solutions of impurities

The Lang section method was actively used to study the decomposition of solid solutions of impurities in semiconductor crystals after their technological treatments, for example, annealing. The papers [53,54] show how the defects formed as a result of silicon annealing affect the visibility of interference fringes in topograms. The annealing duration increasing led to a complete loss of fringes visibility.

First, the decomposition of solid solutions of impurities was studied in silicon crystals grown by the Czochralski method under conditions when it is already well expressed, and there are many defects [35,55,56]. With interest increasing in heavily doped semiconductor crystals, which are actively used in power electronics, the section method began to be used for their diagnostics in the as-grown

state. The developing semiconductor instrument engineering required large-diameter crystals with a high concentration of impurities, approaching the solubility limit, and, at the same time, with high structural perfection. Crystals containing practically no dislocations were obtained. But there was a problem of microdefects generation in them. It turned out that the decomposition of solid solutions of impurities in the form of cluster formation is possible in such crystals already during growth. In the future, it develops with the formation of secondary defects — small dislocation loops, their accumulations, preprecipitations, and precipitates of a new phase. To study these defects the sensitivity of traditional methods for their study was not enough, and more sensitive methods had to be used. The combination of the Lang section method and X-ray diffractometry based on the Bormann effect, i.e., anomalous transmission of X-rays, turned out to be especially effective [57,58]. The beginning of the process of decomposition of solid solutions of impurities can be noticed from the visibility deterioration of the Kato fringes on section topograms and the suppression of the Bormann effect in diffractometry studies. Since the forming defects determine the degradation properties of devices based on these crystals, it is important to control their presence and distribution.

When comparing the results of the Lang section method use together with diffractometric measurements under conditions of the Bormann effect, it was found that in the presence of statistically distributed microdefects in silicon crystals, the fringes in the section topograms disappear at a Debye–Waller factor of $L > 0.017$ [34]. The Debye–Waller factor has the same value when the main defects in silicon are dislocations with the density of $10^3-10^4\,\mathrm{cm}^{-2}$, and fringes are not observed. This value of the Debye–Waller factor can be considered as a measure of the Lang section method sensitivity to the violation of the average lattice due to the presence of microdefects in the crystal. Thus, a qualitative test for the structural perfection of crystals, i.e. observation of the Kato fringes on section topograms, acquires a quantitative expression through the value of the Debye–Waller factor and indicates the absence of microdefects in the crystal in a noticeable amount.

Based on the analysis of the data obtained, the following general conclusions can be made. The presence of statistically distributed microdefects in crystals affects the periodicity change, shape, and intensity of fringes in section topograms. In theory the structure factor F_h is replaced by F_hE_h, where $E_h = \exp(-L_h)$. Here L_h — the Debye–Waller statistical factor, X-ray intensity is multiplied by E_h^2, the Kato fringes period decreases as $1/E_h$, since the argument of the Bessel function is multiplied by E_h. These conclusions are the key to understanding how the presence of statistically distributed microdefects in crystals affects the periodicity change, shape, and intensity of fringes in section topograms.

The Lang section method can be recommended for the diagnostics of heavily doped crystals that do not contain dislocations or contain few dislocations before heat treatments, in the as-grown state. Paper [59] describes a study that showed how, using diffraction methods, one can choose the best heat treatment mode for silicon in terms of the formation and distribution of defects in boron-doped crystals when creating various devices based on them. We studied silicon crystals with a diameter of 150 mm, doped with boron in the process of growing by the Czochralski method to a concentration of $(4-6.5)\cdot 10^{18}\,\mathrm{cm}^{-3}$, subjected to two standard heat treatment modes: ASTM, A and C. Here A is annealing at $T = 1050^\circ$C for 16 h at 5% nitrogen in oxygen atmosphere. Mode C is slow heating up to 800°C for 4 h plus annealing according to mode A (the stage of low-temperature nucleation is added). ASTM is an international standardization system (American Standard Test Method). Its requirements are specified in the description of the treatment modes of silicon samples. Projection topograms and a set of section topograms obtained from samples processed according to A and C modes were compared.

The samples were round disks, which are cross-sections of a silicon ingot. The photographs were taken near the side surface of the disks, in areas where the decomposition of solid solutions of impurities is most pronounced. For mode A the main details of the images of the Kato fringes were preserved on section topograms, despite the superposition of images of microdefects on them, and for mode C they were absent. One can also clearly see the difference in the distribution and size of microdefects after two modes of crystal treatment (Fig. 18).

This showed that in the samples processed according to C mode there are many small defects, and there are practically

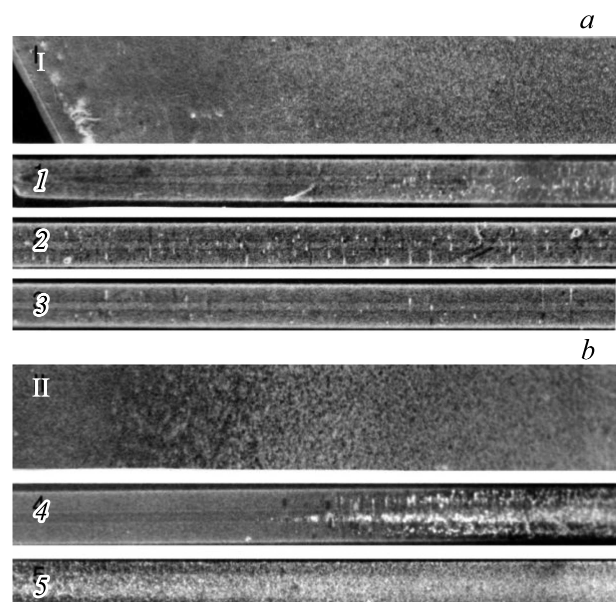

Figure 18. A series of topograms of crystals processed according to A (a) and C (b) modes. I, II — fragments of projection topograms, $1-5$ — section topograms corresponding to projection topograms in the direction from left to right. All topograms were obtained in reflection 220 and radiation MoK_α. The diffraction vector is directed vertically from top to bottom. Section topograms are magnified by two times ($30\times$) in comparison with projection topograms ($15\times$).

no large defects, with the exception of a circular zone near the side surface of the ingot. The qualitative characteristics of the samples structure were supplemented by quantitative data obtained from the analysis of diffuse scattering. The concentration and average size of dislocation loops along the growth axis and along the diameter of the ingot [59,60] were calculated.

The results obtained made it possible to make a confident choice between two modes of silicon heat treatment in terms of the formation and distribution of microdefects. Considering the non-destructive nature of the methods used in the study, they can be recommended for improving the growth and more rational use of crystals in the production of semiconductor devices.

2.3. Investigation of technological defects in crystals

The Lang section method is long been used to study technological defects in crystals that occur during their treatment, and use in semiconductor instrument engineering. At the same time, computer simulation of images of crystal lattice violations is rarely, but still, used to obtain quantitative information about them. In paper [61], based on the analysis of the interference fringes distribution on the Lang section topogram, the force of surface compression in an ion-implanted silicon layer was determined. Boron ions with the energy of 50 keV at a dose of $10^3\,\mathrm{mcc}\cdot\mathrm{cm}^{-2}$ were implanted into a triangular region on the surface of the silicon crystal. The best agreement between experiment and calculation was obtained at a compression force of $3.5\cdot10^4\,\mathrm{dyn}\cdot\mathrm{cm}^{-1}$. However, in most papers the study of technological defects in crystals by the section method is not associated with the observation of interference fringes, but with the possibility of determining the position of individual defects, as well as any boundaries in the bulk of crystals and through their thickness. The use of this method in such aspect is especially effective when studying the effect of impurities gettering. This effect is actively used in the creation of semiconductor devices and can be of two types: external and internal.

The external effect is achieved by the targeted deterioration of the structural state of the surface (for example, by grinding it) and subsequent annealing, as a result of which, due to the formed sinks for point defects, the near-surface region of the crystals is excused from defects. It is important to determine its thickness and „cleanliness" (i.e., whether single defects remain in it). The internal effect of gettering is achieved by the special technological treatment of crystals without disturbing the surface. Paper [62] reviews the typical technological problems when using XT section methods in their solution. The advantages and disadvantages of the methods in two diffraction geometries, i.e. transmission and reflection, are discussed (see below).

The use of Lang section method is often effective in studying systems substrate–epitaxial layer, especially if

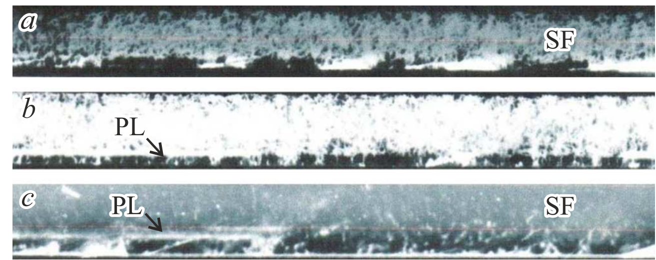

Figure 19. Fragments of section topograms of the composition: substrate $4H$-SiC — porous layer — homoepitaxial layer in transmission (a, b) and reflection (c) geometry. Radiation $\mathrm{Mo}K_\alpha$. Reflections $30\bar{3}0$ (a), $22\bar{4}0$ (b), 0006 (c). SF — stacking faults, PL — porous layer. Positive contrast, magnification 30×.

the substrate contains many defects, and there are no interference fringes in the topogram (Fig. 19). On the shown topograms of the system consisting of the substrate $4H$–SiC — porous layer–homoepitaxial layer, the layer boundaries are visible. It is clearly seen that the structure of the homoepitaxial layer is much more perfect than the structure of the substrate, but the layer contains large stacking faults that originate at the interface with the substrate and grow through the entire thickness of the layer.

Such results could only be obtained by section methods due to the ability of these methods to identify the position of defects and boundaries through the thickness of the samples [63,64]. To analyze the perfection of the structure of objects with epitaxial layers, the section method in Bragg geometry is successfully used. With its help, the structure of near-surface layers is characterized, and the bending radius of objects as a whole is determined. In some problems this method has advantage over the Lang section method. This is demonstrated in Fig. 20 [62] using the example of studying the external and internal effect of gettering in silicon crystals. Due to the lower sensitivity of this method to crystal lattice stresses and, accordingly, the smaller image width of individual defects, the accuracy of determining the position of defects and boundaries turns out to be much higher, up to $0.1a$, where a is the width of the incident beam [65]. Besides, it is possible to determine whether there is a bend in such objects.

The authors of this work used in their studies a special device i.e., the so-called slitless collimator. It made it possible to form very narrow ray beams being incident on the objects of study. With its help they solved many applied problems of microelectronics: determination of the structure of the stress field in crystals as a result of scribing; study of the growth of substrate defects in the autoepitaxial layer on silicon; detection of defects resulting from the surface diffusion of impurities; detection of defects in thin membranes, etc.

It is well known that with significantly different treatment of opposite surfaces of a thin crystal plate (for example, polishing one and grinding the opposite), it acquires a bend.

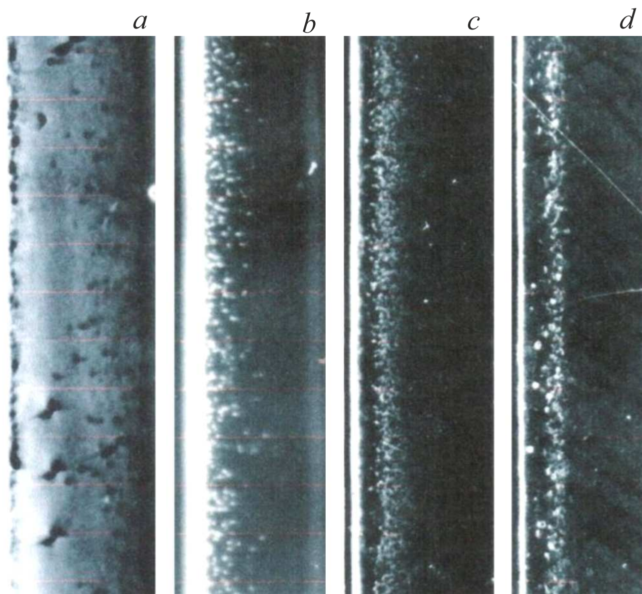

Figure 20. Fragments of section topograms in the Bragg geometry of silicon samples with external (a, b) and internal (c, d) effects of impurity gettering. The topograms were obtained from opposite surfaces of the same sample (a, b) in reflection 333 and from the one surface in different reflections: 800 (c) and 440 (d). Radiation MoK_α. Magnification 30×.

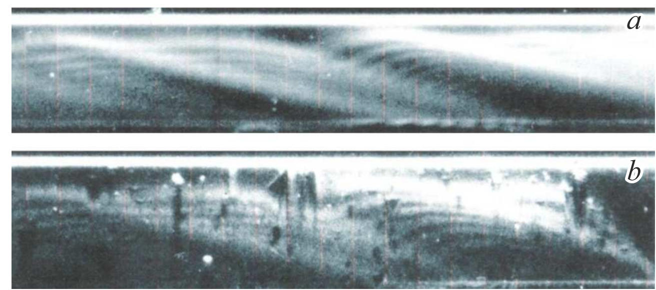

Figure 21. Fragments of section topograms in the reflection geometry of a silicon crystal after local implantation of oxygen ions (a) and a series of post-implantation annealings (b). MoK_α, reflection 333, magnification 30×. The diffraction vector is directed vertically from top to bottom.

It is very small, no deformation fringes are observed in the topogram, and it is not possible to measure its magnitude, but it is possible to determine the sign of the bend from the characteristic contrast of the defects image in the near-surface region of the plate. It corresponds to the convexity of the ground surface and the concavity of the polished one. The defects image contrast in near-surface regions has the opposite sign in topograms obtained by the reflection of X-rays from opposite crystal surfaces. Fragments of topograms in Fig. 20 can serve as an example. They are presented in positive contrast: most of the defect images have a white contrast, as the boundaries of the topograms, which correspond to the total reflection of the incident beam from the crystal surface. In negative contrast it is black. And on the topogram in Fig. 20, *a* the main contrast of defects preserved in the „defect-free zone"is opposite. This observation is characteristic for samples with external effect of impurity gettering due to the significantly different treatment of opposite crystal surfaces. The possibility of determining the sign of the crystal bending from the contrast of the defects image relates to the effect of different focusing of waves propagating in the crystal with bending of the opposite sign, which was described above in the first part of the review.

Interference fringes on section topograms in Bragg geometry were experimentally observed for the first time in bent silicon crystals in [40], then in [66] and in the studies of other researchers. In [42,43] the formation of fringes is explained on the basis of the theory of Bragg reflection of X-rays in crystals with a constant deformation gradient. It is proposed to call these fringes as deformation fringes. This name is now established. It was shown that the deformation fringes appear on section topograms, starting from a certain threshold distance from the main maximum of X-ray reflection from the crystal surface in the form of a fringe of intense black contrast: the first at a distance of $x_1 = (16\pi/5B^2)^{1/3}$, and the subsequent ones — according to the law $x_n \sim (n-1/2)^{1/3}$. Thus, the law of periodicity of fringes was established. The deformation gradient relates to the curvature of the crystal by the relation

$$B \approx \frac{\Lambda^2}{d} \frac{\cos^2\theta}{2\pi\gamma_0\gamma_h} \frac{1}{R}, \tag{5}$$

where Λ — extinction length, d — interplanar distance, θ — Bragg angle; γ_0, γ_h — direction cosines of the incident and reflected beams. For symmetric diffraction $\gamma_0 = |\gamma_h| = \cos\theta$. Based on formula (5) it is possible to determine the radius of curvature of the crystal. It is also shown there that in silicon crystals with a constant deformation gradient the bending manifests itself as deformation fringes on section topograms in Bragg geometry at a critical value of the deformation gradient $B_{\text{cr}} = 16\pi/5t_0^3)^{1/2}$, where t_0 is the absorption length. These formulas can be used to quantify the bending of the crystal.

The section method in Bragg geometry was actively used in the study of crystal lattice stresses associated with the implantation of high-energy ions and particles. In [67], in the region of local implantation of oxygen ions with the energy of 5.15 MeV into silicon, two systems of deformation fringes were found, against the background of which images, after a series of heat treatments, the characteristic images of precipitates appeared as a result of the decomposition of a solid solution of impurities. They had a conical shape elongated in the direction of the diffraction vector (Fig. 21), which is typical for images of point defects in crystals with a bend (see Section 1). Such images can be calculated in the stress field estimated from the bending radii measured on the topograms. This is a rare case of coincidence of

favorable conditions for this kind of studies using numerical simulation.

3. Examples of use of synchrotron radiation in section topography methods

There is an opinion that the use of synchrotron radiation (SR) has radically changed the methods of XT. However, section methods fundamentally changed very little, although they have benefits from the occurrence of intense radiation sources with small angular divergence and transverse coherence. Collimation in the vertical plane, achieved due to the parameters of the SR source, in combination with the small angular size of the source in the horizontal plane makes it possible to use large distances from the source to the sample to increase the illuminated area without the loss of the intensity available near the beam extraction systems. At that, the angular width of the source, visible from a point on the sample, is close to the width of the dynamic diffraction region of the crystal. Owing to the long coherence length on synchrotrons of the third generation, a narrow beam retains the properties of coherence and parallelism within a slit several tens of microns in size. Moreover, it is possible to register topograms at two meter distances from the sample with a high spatial resolution of about few microns. On synchrotrons of moderate brightness section methods began to be used, including in polychromatic radiation.

With the use of polychromatic SR, relatively few studies have been performed relating computer simulation of defect images. Paper [68] describes the application of the section topography method in Bragg geometry to study dislocations in silicon substrates and epitaxial layers. The white SR beam from the source DORIS-III, HASYLAB in Hamburg was limited by a slit $5\,\mu$m wide. The thickness of the samples (plates of Si crystals grown by the Czochralski method) was $700\,\mu$m.

The Uragami fringes [20] were clearly visible in most of the reflections registered in the images. The amplitude of the fringes rapidly decreased with the distance from the main fringe corresponding to the narrow beam reflection from the sample surface. Section topograms with images of rectilinear 60° dislocations inclined to the surface were compared with calculated images. The calculations were performed by the numerical integration of the Takagi–Topen equations using computer programs whose algorithms used a constant or variable integration step. The images of dislocations looked like rosettes with black contrast. The calculation results quite well reproduced the features of the rosettes. However, in the bent crystal the calculated patterns did not exactly correspond to the experimental ones. Computer simulation of dislocation images against the background of the fringes caused by bending showed significant differences, namely, in the presence of dislocations the deformation fringes were distorted much more strongly than the Uragami fringes.

The authors concluded that the use of the narrow slit in a white SR beam makes it possible to reveal many characteristic details and observe interference fringes. The Uragami fringes, which are practically invisible in the radiation from laboratory sources, are less sensitive to microstresses around defects than the deformation fringes, and, on the whole, they are less intense.

The study of images of 60° dislocations in bent substrates, misfit dislocations, and precipitates in layered structures suggests that computer simulation of Bragg section topograms provides at least qualitative agreement with experiment. As a result of dislocation rosettes simulation, i.e., images of dislocations emerging on the surface of flat Si plates at a right angle or close to it showed that the contrast is formed due to the additional intensity caused by the decomposition of the wave field around the dislocation core.

K. Veteska et al. [69] studied the effects of germanium segregation in silicon on DESY-HASYLAB source using the SR section method. On the projection topograms the researchers observed a characteristic contrast associated with growth fringes in single crystals of the Si:Ge solid solution. Section topograms of plates $400\,\mu$m thick were recorded in a white SR beam limited by a slit $5\,\mu$m wide. On the topograms obtained in Bragg geometry at glancing incidence angles 4–8°, a cross pattern was clearly visible. It was formed by growth stripes at the places where they intersect with the SR beam and stop fringes at the exit surface of the sample. In this case, the contrast brightness varied from high to low, indicating that the narrow beam penetrated almost the entire thickness of the sample. By double exposure on the same film the combined images were obtained, which were a superposition of section images on projection ones. The photos were registered for different positions of the sample relative to the beam direction, when the sample was rotated by 180° around the normal to the surface, parallel to the growth axis $\langle 111 \rangle$. In another case, the sample was rotated around the $[1\bar{1}0]$ axis perpendicular to the incident beam. In this case, the images of the growth fringes were rotated with respect to the crystal boundary. This made it possible to establish a compliance between the sample surface and the convex-concave growth surface. By comparing the section topograms of samples with higher (3%) and lower (1.2%) Ge concentrations, the authors estimated the range of Si lattice misorientations that contribute to the image contrast of segregation fringes. It was concluded that the contrast well approximated the germanium distribution in Si:Ge ingots grown by the Czochralski method.

In the early 2000s great interest was shown in crystals of indium antimonide (InSb), the direct bandgap zone of which is the narrowest in comparison with other A^3B^5 semiconductors. On the basis of InSb, IR detectors are made, the parameters of which are affected by structural defects. InSb strongly absorbs radiation from X-ray tubes, which makes the topogram registration process long. The acceptable exposure time and obtaining a large number of

topograms on one film at once is ensured by the use of polychromatic SR.

Using ANKA SR source in Karlsruhe, Germany, $p-i-n$-structures based on InSb were studied. Samples fabricated by metal organic vapour phase epitaxy had n-type InSb epitaxial layer on one side of InSb substrate, and a similar p-type layer on the other side. In this case, the layer thickness was 200−300 nm, and the substrate thickness was 600 μm [70].

The section method in Laue geometry revealed the disappearance of the Kato interference fringes pattern in the topograms of samples with a high concentration of impurity atoms. Instead of fringes, black-and-white rounded images of defects in the epitaxial layers appeared on the images. These images were absent on the topograms of the substrates.

To explain the nature of the defects the researchers used the projection topography. By calculating the anomalous absorption coefficient (multiplied by the thickness of the sample), they concluded that for the selected reflections the diffracted beam met the anomalous transmission conditions. The black-and-white contrast of images was explained on the basis of dynamic theory, assuming lattice deformations around pores and precipitates. The lattice bending towards the pore, caused by the tensile deformation, forms an increase of the reflected intensity on one side of the pore and a decrease on the other one. Images of defects near the exit surface of the sample with a white part on the positive side of the diffraction vector **g** correspond to pores. The precipitates have reverse contrast.

This paper was one of the first proofs of the existence of precipitates and pores in InSb epitaxial layers with an estimate of their number. It was concluded that small deviations from the equilibrium ratio of Sb and In atoms in vapor flows during epitaxy cause the atoms clustering on the layer surface. Impurity atoms induced during doping can enhance this effect.

For many years silicon is in the focus of interest in X-ray topographic studies. The focus shift from the study of growth and technological defects to the problems of packaging the integrated circuits is caused by the need to develop devices with increased reliability. A number of problems arise during the operation of microchips fabricated by mounting on contact pads (bumps), for the study of which the authors of paper [71] used the section topography method. The aim of the paper was to evaluate the effectiveness of the method for the detection and analysis of mechanical stresses in Si substrates under contact pads.

The samples for study consisted of the elements shown schematically in Fig. 22, a and listed in the text under the Figure. In the course of experiments in white SR beam, the high-resolution film installed behind the sample recorded rays diffracted in the reverse direction. On the projection topograms the regions with mottled contrast corresponded to different levels of deformation of the Si lattice under the pads, which is caused by intermetallic subgrains in the Ni(P)

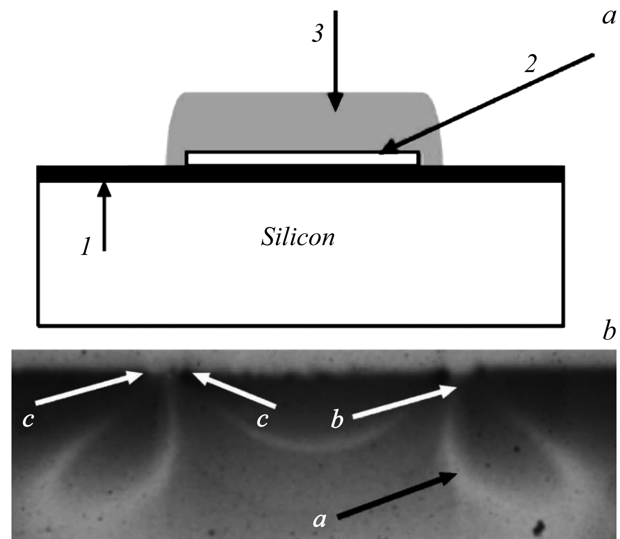

Figure 22. a — circuit of one contact from a series of contact pads distributed over the surface of the chip crystal. Above the Si substrate with an oxide (*1*) and aluminum (*2*) layer a platform with Ni(P) (*3*) metallization layer protrudes; b — section topogram in reflection $1\bar{1}5$ from the area with a diameter and thickness of 600 and 2.9 μm, respectively [71].

metallization layers. The greatest distortions were localized near the periphery of the pad.

To make section topograms the beam was limited by a slit 20 μm wide. Each reflection on the Laue photograph indicated deformations distributed through the thickness of the substrate. By comparing reflections with different penetration depth of radiation into the sample, it was found that strong long-range stresses (arrow a, Fig. 22, b) come from the regions under the periphery of the pad, where the deformation centers have a reduced (black) contrast (arrows b and c).

The authors determined the maximum misorientation angle of Si lattice under the pads. The deformation was converted to stress under the assumption that the misorientation is caused by shear stresses near the interface. For pads with a diameter of 200 μm, the stress did not exceed 65 MPa. However, for pads with a diameter of 800 μm, the stress increased to 260 MPa. Thus, with the help of X-ray topography alone the important conclusion was made. During the development of integrated circuit packaging technologies, the benefits and losses must be compared. On the one hand, the advantage of a large soldered joint diameter is to reduce the temperature of the soldered junction. On the other hand, the size increasing of the contact pads increases the stresses in Si substrates.

The study of plastic deformation processes in the bulk of large crystals without their destruction is a serious problem. A group of experimenters headed by J. Baruchel at the ID-19 beamline of ESRF (European Synchrotron Radiation Facility) in Grenoble, France, studied growth defects in $4H$−SiC crystals by topography in white SR without thin

plates preparation [72,73]. The samples were ingots with a diameter of 35 mm and height of 12 mm. The SR beam was limited by slit with a width of 50 μm, which made it possible to avoid the superposition of images of many defects in the sample bulk on one 2D projection [5]. The film registered images of defects inside the layer corresponding to the cross-section of the crystal by a narrow SR beam. The exposure time did not exceed 10 s. The spatial resolution of the scheme was 5 μm. Section topograms in Laue geometry were obtained at four different positions of the sample. In particular, the registration of images under conditions, where the orientation of the growth axis is parallel to the plane of incidence of the SR beam, identified the defects propagation during crystal growth. The interface between the crystal and the seed was barely noticeable, indicating a smooth start at the beginning of growth. However, with growth the inclusions of foreign polytypes were formed: $6H-$SiC or $15R-$SiC. They originated on one side of the ingot and propagated into the bulk until they reached the other side. In this case, planar defects of the type of 2D grain boundaries appeared. The study of different ingots showed that polytype inclusions, as a rule, were overgrown. However, the grain boundaries had a negative effect on the structural perfection of a significant part of the sample bulk. Thus, the XT method identified important features of the defect structure formation of $4H-$SiC crystals before they were used to prepare substrates for electronic devices.

For a long time, the reliability of electronic devices based on SiC was degraded by micropipes i.e. hollow cores of screw superdislocations with giant Burgers vectors. These pores were „fatal" for the operation of devices, causing the breakdown of microplasma [74]. Thanks to the optimization of the technology for obtaining bulk SiC single crystals, the industrial production of substrates that do not contain micropipes [75,76] was successfully implemented. However, substrates contain dislocations, and it is still not entirely clear which types of dislocations are most detrimental to devices operation. A group of researchers headed by D. Nakamura studied the behavior of dislocations in $4H-$SiC using the direct method for determining the Burgers vector [77,78]. The scheme of the section method of topography in white SR beam was similar to that used earlier to study superdislocations in $6H-$SiC [79]. However, the distance from the sample to the film was increased by more than 10 times. Due to the high SR brightness and the small size of the source on the beamline of the SPring-8 facility, the distance increasing did not lead to quality deterioration of X-ray topograms.

On the projection topograms the lines of screw dislocations were oriented along the crystal growth direction, which formed the angle 8° with the axis $\langle 0001 \rangle$. Section topograms in Laue geometry were registered in SR beam limited by a slit of 30 μm onto a film in 2 m away from the sample. The resolution on the topogram calculated from the angular width of the source was 7 and 1 μm, respectively, in the horizontal and vertical directions. Images of screw dislocations on section topograms had hyperbolic profile, which was explained in detail in the paper of A.R. Lang et al. [80]. The calculated profile of the dislocation image with the Burgers vector $b = 1c$, where c is the lattice parameter $4H-$SiC, was in good agreement with the experiment. The main conclusion of this paper relates to left and right elementary dislocations. The authors found that neighboring screw dislocations have a trend to have different signs. In their opinion, the probable cause of this effect is the contactless elastic interaction between screw dislocations separated by a distance of at least 200 μm. Long-range interaction can affect the nature of propagation and distribution of elementary dislocations.

In this Section we consider the results of studies of various practically important crystals with structural defects in order to show the variety of problems that have been solved till present time with the help of SR. Due to short exposures, the section topograms were combined with the projection topograms by double exposure. The continuous spectrum made it possible to obtain many topograms on one film at once. Thanks to the section method, the structural properties of crystals with defects were interpreted. Note that theoretical studies are not limited to the above-described case of computer simulation of section topograms of an almost perfect silicon crystal [68]. Our review does not include the results of analysis of the spherical wave reflection [81] and two-wave diffraction [82] in elastically bent Si plates, as well as experimental studies of new almost perfect single crystals and multilayer structures: vanadites [83] and InGaAs$-$InAlAs [84] superlattices. The use of synchrotron radiation can turn section topography into an express method of non-destructive diagnostics, in particular, into a method for monitoring the bending and warping of silicon crystals in fully packaged semiconductor devices [85].

It should be mentioned that a large number of studies using SR were performed by step-scanning technique stop-frames in combination with linear and/or angular movement of the sample. Having processed the topograms using a visualization program, the experimenters obtained 3D patterns of the defects distribution in the bulk of the crystals [86–90]. However, this is not a quantitative approach. Methods, in which the spherical wave approximation was not performed, were not considered under this review.

Conclusion

Section RT methods are extremely sensitive to weak crystal lattice stresses and have a high potential for developing means for obtaining quantitative information about them. These methods are practically ready for solving complex fundamental and applied problems of materials science. They are based on a well-developed theory. They are based on the experience of previous and current studies. The use of SR increased the possibilities of methods. In particular,

the range of studied materials was expanded. In some cases, it was possible to study defects in crystals in the form of ingots, which allows the experimenter to exclude the special samples preparation. The spatial resolution and brightness of defect images increased. This makes it possible to study the fine details of the technological methods used in the manufacture of microelectronic devices and to improve the technology of instrument engineering. Finally, the use of SR made it possible to clearly observe the Uragami fringes and use them to interpret section topograms in Bragg geometry.

However, it should be recognized that the main achievements in the development and application of section methods are described in studies performed using laboratory radiation sources. In addition to section methods, another method is known in X-ray topography, which is highly sensitive to weak lattice distortions and makes it possible to obtain quantitative information about them. This is quasi-plane wave X-ray topography. The method is so named because the approach to the plane wave is possible in synchrotron radiation only. Although this other method, based on different principles, differs from the section methods and therefore is not discussed in this review, we add to the list of references several important studies performed by quasi-plane wave topography [91–94]. We also add to the list a link to a new effective method for studying defects in crystals, called topo−tomography [95].

At present, thanks to RT section methods the images of many types of defects were calculated, and their models were made. These are still quite simple defects: straight dislocations of various types, located in certain positions in the bulk of crystals, flat stacking faults, etc. The time of more complex types of defects has come: general position dislocations, superdislocations, and micropipes in SiC crystals; bulk stacking faults in SiC and synthetic diamond crystals, etc.

Growth defects in crystals are often decorated with impurities. This changes the stress field associated with defects, affects their properties, and can change the properties of the crystal as a whole. At present, sufficient potential has been accumulated to study this phenomenon on the basis of RT section methods with the use of numerical simulation.

Funding

This research was partially supported by Russian Foundation for Basic Research (RFBR), grant number 19-29-12041 mk.

Conflict of interest

The authors declare that they have no conflict of interest.

References

[1] W. Berg. Naturwissenschaften, **19**, 391 (1931). DOI: 10.1007/BF01522358
[2] W. Berg. Z. Kristallogr., **89**, 286 (1934). DOI: 10.1524/zkri.1934.89.1.286
[3] A.R. Lang. Acta Metall., **5** (7), 358 (1957). DOI: 10.1016/0001-6160(57)90002-0
[4] V.G. Kohn, A. Kazimirov. Phys. Rev. B, **75** (22), 224119 (2007). DOI: 10.1103/PhysRevB.75.224119
[5] V.V. Lider. Phys. Solid State, **63** (2), 189 (2021). DOI: 10.1134/S1063783421020141
[6] V.V. Aristov, V.G. Kohn, V.I. Polovinkina, A.A. Snigirev. Phys. Status Solidi A, **72** (2), 483 (1982). DOI: 10.1002/pssa.2210720207
[7] V.L. Indenbom, F.N. Chukhovsky. UFN, **107** (2), 229 (1972) (in Russian). DOI: 10.3367/UFNr.0107.197206c.0229
[8] E.V. Suvorov, I.A. Smirnova. UFN, **185** (9), 897 (2015) (in Russian). DOI: 10.3367/UFNr.0185.201509a.0897
[9] S. Takagi. Acta Crystallogr., **15**, 1311 (1962). DOI: 10.1107/S0365110X62003473
[10] S. Takagi. J. Phys. Soc. Jpn., **26** (5), 1239 (1969). DOI: 10.1143/JPSJ.26.1239
[11] D. Taupin. Bull. Soc. Franc. Mineral. Crystallogr., **87**, 469 (1964).
[12] D. Taupin. Acta Crystallogr., **23**, 25 (1967). DOI: 10.1107/S0365110X67002063
[13] A. Authier. A Dynamical Theory of X-Ray Diffraction (Science Publ., Oxford, 2001)
[14] Y. Ando, J.R. Patel, N. Kato. J. Appl. Phys., **44** (10), 4405 (1973). DOI: 10.1063/1.1661973
[15] E.V. Suvorov, V.I. Polovinkina, V.I. Nikitenko, V.L. Indenbom. Phys. Status Solidi A, **26** (1), 385 (1974). DOI: 10.1002/pssa.2210260140
[16] A.M. Afanas'ev, V.G. Kohn. Acta Crystallogr. A, **27**, 421 (1971). DOI: 10.1107/S0567739471000962
[17] J. Härtwig. J. Phys. D: Appl. Phys., **34** (10A), A70 (2001). DOI: 10.1088/0022-3727/34/10a/315
[18] N. Kato. Acta Crystallogr., **14**, 526 (1961). DOI: 10.1107/S0365110X61001625
[19] N. Kato. J. Appl. Phys., **39** (5), 2225 (1968). DOI: 10.1063/1.1656535
[20] T. Uragami. J. Phys. Soc. Jap., **27** (1), 147 (1969). DOI: 10.1143/JPSJ.27.147
[21] E.V. Shulakov, I.A. Smirnova. Poverkhnost, **1**, 96 (2001) (in Russian).
[22] A.R. Lang, M. Zhen-Hong. Proc. Roy. Soc A, **368**, 313 (1979). DOI: 10.1098/rspa.1979.0132
[23] F.N. Chukhovskii, K.T. Gabrielan, P.V. Petrashen. Acta Crystallogr. A, **34**, 610 (1978). DOI: 10.1107/S056773947800128X
[24] A. Authier. J.R. Patel. Phys. Status Solidi A, **27** (1), 213 (1975). DOI: 10.1002/pssa.2210270125.
[25] A. Authier. Bull. Soc. Franc. Mineral. Crystallogr., **84** (1), 51 (1961).
[26] F. Balibar, A. Authier. Phys. Status Solidi B, **21** (1), 413 (1967). DOI: 10.1002/pssb.19670210141.
[27] A. Authier. Adv. X-Ray Analysts, **10**, 9 (1967).
[28] Y. Epelboin, A. Authier. Acta Crystallogr. A, **39**, 767 (1983). DOI: 10.1107/S010876738300152X
[29] V.N. Erofeev, V.I. Nikitenko, V.I. Polovinkina, E.V. Suvorov. Kristallografiya, **16** (1), 190 (1971) (in Russian).

[30] E.V. Suvorov, O.S. Gorelik, V.M. Kaganer, V.L. Indenbom. Phys. Status Solidi A, **54** (1), 29 (1979). DOI: 10.1002/pssa.2210540103.
[31] E.V. Suvorov, I.A. Smirnova. Phys. Solid State, **52** (12), 2485 (2010). DOI: 10.1134/S1063783410120073
[32] E.V. Suvorov, I.A. Smirnova, E.V. Shulakov. Poverkhnost, **9**, 64 (2004) (in Russian).
[33] E.V. Suvorov, I.A. Smirnova, E.V. Shulakov. Poverkhnost, **4**, 100 (2004) (in Russian).
[34] R.N. Kyutt, S.S. Ruvimov, I.L. Shulpina. Tech. Phys. Lett., **32** (12), 1079 (2006). DOI: 10.1134/S106378500612025X
[35] M.G. Milvidsky, Yu.A. Osipyan, E.V. Suvorov, I.A. Smirnova, E.V. Shulakov. Poverkhnost, **6**, 5 (2001) (in Russian).
[36] I.L. Shulpina, E.V. Suvorov. Bull. Russ. Acad. Sci. Phys., **74** (11), 1488 (2010).
[37] F. Heyroth, H.-R. Höche, C. Eisenschmidt. J. Appl. Crystallogr., **32**, 489 (1999). DOI: 10.1107/S002188989900240X
[38] V.G. Kohn, I.A. Smirnova. Acta Crystallogr. A, **71**, 519 (2015). DOI: 10.1107/S2053273315012176
[39] E.V. Shulakov, I.A. Smirnova, E.V. Suvorov. Poverkhnost, **6**, 5 (2003) (in Russian).
[40] P. Zaumseil. Krist. Tech., **13** (8), 983 (1978). DOI: 10.1002/crat.19780130814
[41] I.L. Shulpina, P.V. Petrashen, F.N. Chukhovsky, K.T. Gabrielyan. Tez. dokl. IV Vsesoyuznogo soveschaniya „Defekty struktury v poluprovodnikakh" (Novosibirsk, SSSR, 1984), t. 2, s. 114 (in Russian).
[42] P.V. Petrashen, F.N. Chukhovsky, I.L. Shulpina, R.N. Kyutt. FTT, **29** (5), 1608 (1987) (in Russian).
[43] F.N. Chukhovskii, P.V. Petrashen. Acta Crystallogr. A, **44**, 8 (1988). DOI: 10.1107/S0108767387005099
[44] E.V. Suvorov, I.A. Smirnova, A.S. Obrazova. Instruments Experiment. Tech., **58** (1), 170 (2015). DOI: 10.1134/S0020441215010297
[45] I.A. Smirnova, E.V. Suvorov, E.V. Shulakov. Phys. Solid State, **53** (1), 35 (2011). DOI: 10.1134/S1063783411010288
[46] E.V. Suvorov, I.A. Smirnova. Tech. Phys. Lett., **42** (9), 955 (2016). DOI: 10.1134/S1063785016090261
[47] V.L. Indenbom, F.N. Chukhovsky. Kristallografiya, **16** (6), 1101 (1971) (in Russian).
[48] B.K. Tanner. X-ray Diffraction Topography (Pergamon Press, Oxford, 1976)
[49] S.F. Cui, G.S. Green, B.K. Tanner. Mater. Res. Soc. Symp. Proc., **138**, 71 (1989). DOI: 10.1557/PROC-138-71
[50] I.L. Shulpina. Poverkhnost, **4**, 3 (2000) (in Russian).
[51] S.Yu. Martyushov, N.V. Kornilov, S.N. Polyakov, S.I. Zholudev, A.A. Lomov, I.L. Shulpina. *Tez. dokl. 8 Mezhdunar. konf. „Kristallografika i deformatsionnoe povedenie perspektivnykh materialov"* (Moskva, Rossiya, 2019), s. 153 (in Russian). DOI: 10.26201/ISSP.2019.45.557/Def.Mater.132
[52] S.N. Polyakov, A.A. Lomov, I.L. Shulpina, S.Yu. Martyushov, V.N. Denisov, V.D. Blank. *Tez. dokl. konferentsii „Elektronno-luchevye tekhnologii i rentgenovskaya optika v mikroelektronike"* (Chernogolovka, Rossiya, 2021), s. 268 (in Russian).
[53] J.R. Patel. J. Appl. Phys., **44** (9), 3903 (1973). DOI: 10.1063/1.1662869
[54] D.K. Bowen, B.K. Tanner. *High Resolution X-ray Diffractometry and Topography* (Taylor and Francis, London, 1998).
[55] M. Lefeld-Sosnowska, J. Gronkowski, G. Kowalski. J. Phys. D: Appl. Phys., **28** (4A), A42 (1995). DOI: 10.1088/0022-3727/28/4A/008
[56] P. Klang, V. Holý, J. Kuběna, R. Štoudek, J. Šik. J. Phys. D: Appl. Phys., **38** (10A), A105 (2005). DOI: 10.1088/0022-3727/38/10A/020
[57] S. Rouvimov, R. Kuytt, J. Kearns, V. Todt, B. Orschel, H. Siriwardane, A. Buczkowski, I. Shul'pina, G.A. Rozgonyi. Solid State Phenomena, eds. H. Richter, M. Kittler, **95–96**, 17 (2004). DOI: 10.4028/www.scientific.net/SSP.95-96.17
[58] R.N. Kyutt, I.L. Shulpina, G.N. Mosina, V.V. Ratnikov, L.M. Sorokin, M.P. Scheglov, S.S. Ruvimov, J. Kearns, V. Todt. J. Phys. D: Appl. Phys., **38** (10A), A111 (2005). DOI: 10.1088/0022-3727/38/10A/021
[59] I.L. Shulpina, S.S. Ruvimov, R.N. Kyutt. Poverkhnost, **1**, 38 (2010) (in Russian).
[60] I.L. Shul'pina, R.N. Kyutt, V.V. Ratnikov, I.A. Prokhorov, I.Zh. Bezbakh, M.P. Shcheglov. Tech. Phys., **55** (4) 537 (2010). DOI: 10.1134/S1063784210040183
[61] P.V. Petrashen, I.L. Shulpina. Phys. Status Solidi A, **78** (2), K105 (1983).
[62] I.L. Shulpina. Zavodskaya laboratoriya, **73** (5) 30 (2007) (in Russian).
[63] I.L. Shulpina, V.V. Ratnikov, N.S. Savkina, V.B. Shuman, M. Syvajarvi, R. Yakimova. Materials Science Forum, **483–485**, ed. R. Nipoti, A. Poggi, A. Scorzoni. Switzerland, Trans Tech Publ. Ltd, 2005, 265–268. DOI: 10.4028/www.scientific.net/MSF.483-485.265
[64] I.L. Shulpina, V.V. Ratnikov, N.S. Savkina, V.B. Shuman. Poverkhnost, **6**, 18 (2005) (in Russian).
[65] I.N. Leikin, K.L. Golovchiner, T.A. Mingazin. Poverkhnost, **9**, 136 (1984) (in Russian).
[66] H. Chen. Mater. Lett., **4** (2), 65 (1986). DOI: 10.1016/0167-577X(86)90051-0
[67] I.L. Shulpina, N.S. Zhdanovich, V.I. Sokolov. Elektronnaya tekhnika, **4** (241), 48 (1989) (in Russian).
[68] W. Wierzhowski, K. Wieteska, W. Graeff. J. Phys. D: Appl. Phys., **33** (10), 1230 (2000). DOI: 10.1088/0022-3727/33/10/314
[69] K. Wieteska, W. Wierzhowski, W. Graeff, M. Lefeld-Sosnowska, M. Regulska. J. Phys. D: Appl. Phys., **36** (10A), A133 (2003). DOI: 10.1088/0022-3727/36/10A/327
[70] J. Riikonen, T. Tuomi, A. Lankinen, J. Sormunen, A. Säynätjoki, L. Knuuttila, H. Lipsanen, P.J. Mcnally, L. O'Reilly, A. Danilewsky, H. Sipilä, S.Vaijärvi, D. Lumb, A. Owens. J. Mater. Sci-Mater. El., **16**, 449 (2005). DOI: s10854-005-2313-5
[71] D. Noonan, P.J. McNally, W.-M. Chen, A. Lankinen, L. Knuuttila, T.O.Tuomi, A.N. Danilewsky, R. Simon. Microelectr., **37** (11), 1372 (2006). DOI: 10.1016/j.mejo.2006.06.008
[72] E. Pernot, P. Pernot-Rejmankova, M. Anikin, B. Pelissier, C. Moulin, R. Madar. J. Phys. D: Appl. Phys., **34** (10A), A136 (2001). DOI: 10.1088/0022-3727/34/10A/328
[73] J. Baruchel, M. Di Michiel, T. Lafford, P. Lhuissier, J. Meyssonnier, H. Nguyen-Thi, A. Philip, P. Pernot, L. Salvo, M. Scheel. C.R. Physique, **14** (2–3), 208, (2013). DOI: 10.1016/j.crhy.2012.10.010
[74] P.G. Neudeck, J.A. Powell. IEEE Electr. Device L., **15** (2), 63 (1994). DOI: 10.1109/55.285372

[75] St.G. Müller, M.F. Brady, A.A. Burk, H. Md. Hobgood, J.R. Jenny, R.T. Leonard, D.P. Malta, A.R. Powell, J.J. Sumakeris, V.F. Tsvetkov, C.H. Carter. Superlattice Microst., **40** (4–6), 195 (2006). DOI: 10.1016/j.spmi.2006.09.029
[76] P.J. Wellmann. Semicond. Sci. Technol., **33**, 103001 (1–34) (2018). DOI: 10.1088/1361-6641/aad831
[77] D. Nakamura, S. Yamaguhi, Y. Hirose, T. Tani, K. Takatori. J. Appl. Phys., **103** (1), 013510 (1–7) (2008). DOI: 10.1063/1.2829806
[78] D. Nakamura, I. Gunjishima, S. Yamaguhi, T. Ito, A. Okamoto, H. Kondo, S. Onda, K. Takatori. Nature, **430**, 1009 (2004). DOI: 10.1038/nature02810
[79] W. Si, M. Dudley, R. Glass, V.Tsvetkov, C. Carter. J. Eletron. Mater., **26**, 128 (1997). DOI: 10.1007/s11664-997-0138-0
[80] S. Mardix , A. R. Lang, I. Blech. Phil. Mag., **24**, 683 (1971). DOI: 10.1080/14786437108217039
[81] H. Yan, Ö. Kalenci, I.C. Noyan. Appl. Crystallogr., **40**, 322 (2007). DOI: 10.1107/S0021889807003160
[82] T. Fukamachi, S. Jongsukswat, D. Ju, R. Negishi, K. Hirano, T. Kawamura. Acta Crystallogr. A, **75**, 842 (2019). DOI: 10.1107/S2053273319011859
[83] M.B. Kosmyna, B.P. Nazarenko, V.M. Puzikov, A.N. Shekhovtsov, W. Paszkowicz, A. Behrooz, P. Romanowski, A.S. Yasukevich, N.V. Kuleshov, M.P. Demesh, W. Wierzchowski, K. Wieteska, C. Paulmann. J. Cryst. Growth, **445**, 101, (2016). DOI: 10.1016/j.jcrysgro.2016.04.002
[84] W. Wierzchowski, K. Wieteska, J. Gaca, M. Wójcik, M. Mozdzonek, W. Strupiński, M. Wesołowski, C. Paulmann. J. Appl. Crystallogr., **50**, 1192 (2017). DOI: 10.1107/S1600576717008846
[85] B.K. Tanner, P.J. McNally, A.N. Danilewsky. Powder Diffr., **36** (2), 78 (2021). DOI: 10.1017/S088571562100021X
[86] W. Ludwig, P. Cloetens, J. Härtwig, J. Baruchel, B. Hamelin, P. Bastie. J. Appl. Crystallogr., **34**, 602 (2001). DOI: 10.1107/S002188980101086X
[87] S. Kawado, T. Taishi, S. Iida, Y. Suzuki, Y. Chikaura, K. Kajiwara. J. Synchrotron Rad., **11**, 304 (2004). DOI: 10.1107/S0909049504012609
[88] T. Mukaide, K. Kajiwara, T. Noma, K. Takada. J. Synchrotron Rad., **13**, 484 (2006). DOI: 10.1107/S090904950603384X
[89] V.V. Kvardakov, K.M. Podurets, S.A. Schetinkin, J. Baruchel, J. Härtwig, M. Schlenker. Nucl. Instrum. Meth. Phys. Res. A, **575** (1–2), 140 (2007). DOI: 10.1016/j.nima.2007.01.044
[90] K. Kajiwara, S. Kawado, S. Iida, Y. Suzuki, Y. Chikaura. Phys. Status Solidi A, **204** (8), 2682 (2007). DOI: 10.1002/pssa.200675677
[91] A.E. Voloshin, I.L. Smol'skii, V.N. Rozhanskij. ZhTF, **64** (4), 171 (1992) (in Russian).
[92] A.E. Voloshin, I.L. Smolsky, V.M. Kaganer, V.L. Indenbom, V.N. Rozhansky. Phys. Status Solidi A, **130** (1), 61 (1992). DOI: 10.1002/pssa.2211300108
[93] A.E. Voloshin. Cryst. Rep. **56** (5) 802 (2011). DOI: 10.1134/S1063774511050233
[94] I.L. Smolsky, A.E. Voloshin, N.P. Zaitseva, E.B. Rudneva, H. Klapper. Philos. Tr. Soc. Lond, A. **357**, 2631 (1999). DOI: 10.1098/rsta.1999.0453
[95] V. Asadchikov, A. Buzmakov, F. Chukhovskii, I. Dyachkova, D. Zolotov, A. Danilewsky, T. Baumbach, S. Bode, S. Haaga, D. Hänschke, M. Kabukcuoglu, M. Balzer, M. Caselle, E. Suvorov. J. Appl. Cryst., **51**, 1616 (2018). DOI: 10.1107/S160057671801419X